The Astrophysical Journal, 846:86 (17pp), 2017 September 1 https://doi.org/10.3847/1538-4357/aa7de4

Exploring the Inner Acceleration Region of Solar Wind: A Study Based on Coronagraphic UV and Visible Light Data

A. Bemporad
Istituto Nazionale di Astrofisica (INAF), Osservatorio Astrofisico di Torino, via Osservatorio 20, I-10025 Pino Torinese, Torino, Italy; bemporad@oato.inaf.it
Received 2017 February 24; revised 2017 June 30; accepted 2017 June 30; published 2017 September 1

Abstract

This work combined coronagraphic visible light (VL) and UV data to provide with an unprecedented view of the inner corona where the nascent solar wind is accelerated. The UV (H I Lyα) and VL (polarized brightness) images (reconstructed with *SOHO*/UVCS, LASCO, and Mauna Loa data) have been analyzed with the Doppler dimming technique to provide for the first time daily 2D images of the radial wind speed between 1 and 6 $R_\odot$ over 1 month of observations. Results show that both polar and equatorial regions are characterized at the base of the corona by plasma outflows at speeds >100 km s^{-1}. The plasma is then decelerated within ~1.5 $R_\odot$ at the poles and ~2.0 $R_\odot$ at the equator, where local minima of the expansion speeds are reached, and gently reaccelerated higher up, reaching speeds typical of fast and slow wind components. The mass flux is highly variable with latitude and time at the equator and more uniform and stable over the poles. The polar flow is asymmetric, with speeds above the south pole lower than those above the north pole. A correlation (anticorrelation) between the wind speed and its density is found below (above) ~1.8 $R_\odot$. The 2D distribution of forces responsible for deceleration and reacceleration of solar wind is provided and interpreted in terms of Alfvén waves. These results provide a possible connection between small-scale outflows reported with other instruments at the base of the corona and bulk wind flows measured higher up.

Key words: solar wind – Sun: corona – Sun: UV radiation – techniques: spectroscopic

Supporting material: animations

1. Introduction and Motivations for this Study

After many decades of theoretical and observational studies on the problem of the solar wind acceleration, many points are still waiting for major clarifications. One of them is a full identification of the region in the inner corona where the larger fraction of solar wind acceleration occurs for both the fast (v > 500 km s^{-1} at 1 au) and slow (v < 500 km s^{-1} at 1 au) wind components. The main hurdle to solving this problem is to obtain reliable measurements of the wind speed in the inner corona (i.e., at heliocentric distances between 1 and ~10 $R_\odot$) for different species in the coronal plasma (protons, electrons, alpha particles, and heavy ions). Moreover, because the wind acceleration problem is strictly related to physical processes responsible for energy deposition in the corona, and hence for coronal heating, a full understanding of solar wind acceleration requires reliable measurements of kinetic temperatures of the same species. Nevertheless, for many different reasons, these measurements are difficult to obtain over such a broad altitude interval, even combining space-based and ground-based remote sensing observations acquired at many different wavelength intervals going from radio to visible and UV domains.

More in detail, the fast and slow wind speeds in the acceleration region have been directly measured using three different techniques. The first one is based on the assumption that small-scale (~100 km) density irregularities propagating with the solar wind can be used as tracers of the local plasma speed. The speed of these density irregularities can be measured from the time delay of interplanetary radio scintillation induced over different compact radio sources, by using both natural (e.g., Scott et al. 1983) and spacecraft (e.g., Woo & Martin 1997) radio sources. This technique was successfully applied in the altitude interval between ~5 and ~100 $R_\odot$, hence usually missing the inner acceleration region located at altitudes <5 $R_\odot$ because of strong scattering of radio waves closer to the Sun; only quite recently was the same technique extended for the first time down to 1.5 $R_\odot$ (see Imamura et al. 2014). A second technique is based on the assumption that small-scale (~10^3–10^4 km) plasma blobs or moving coronal features observed in visible light (VL) coronagraphic images can be used again as tracers of the local plasma speed (Sheeley et al. 1997). This technique has been successfully applied in the altitude interval between ~2 and ~30 $R_\odot$, but missing again the inner acceleration region located below the edge of the external occulter of coronagraphs (<2 $R_\odot$), where these observations are not available; the same technique was also improved by using correlation tracking (Lewis & Simnett 2000, 2002). Results show that these blobs are formed and/or start to accelerate around an altitude of 2.5–4.5 $R_\odot$, having a near-zero velocity below that altitude. A third technique (which will be quickly reviewed in the next paragraph of this paper) is based on the so-called Doppler dimming technique (Withbroe et al. 1982; Noci et al. 1987) applied to UV spectroscopic observations and aimed at measuring directly the proton and heavy ion expansion speed (Antonucci 2006; Kohl et al. 2006), under the assumption that effects related to the line-of-sight integration can be taken into account (see Raouafi & Solanki 2004; Cranmer et al. 2008). Since 1996, the inner solar wind acceleration region was deeply explored with the UV Coronagraph Spectrometer (UVCS) instrument (Kohl et al. 1995) on board the ESA-NASA *Solar and Heliospheric Observatory* (*SOHO*). One of the main advantages of this instrument (operating until 2012) was its capability of obtaining at the same time measurements of outflow velocities and kinetic temperatures for different species over a broad altitude interval and at different latitudes in the inner corona, thus providing unique information for both the wind acceleration and coronal heating problems. A comprehensive view of proton outflow

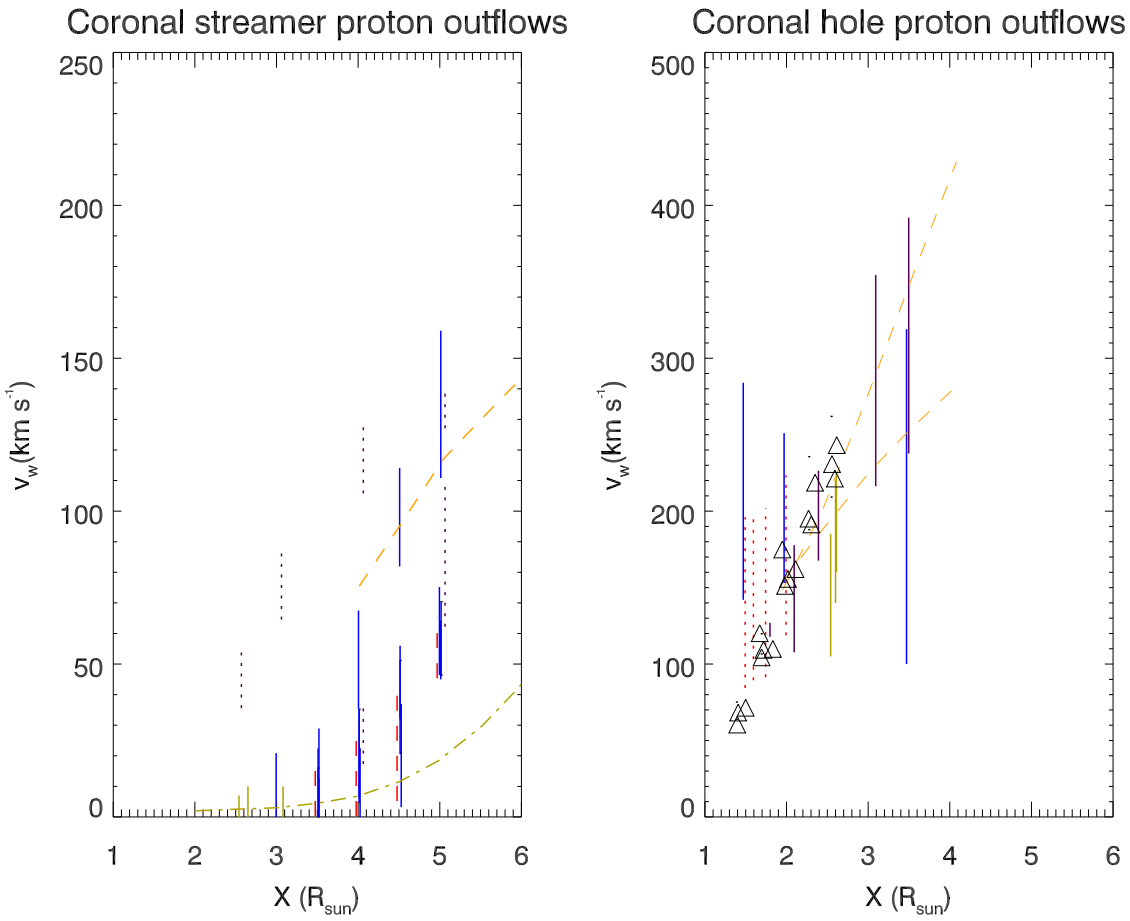

Figure 1. Compilation of neutral H outflow speeds (usually assumed to represent the proton outflow speeds) measured with the analysis of UVCS data acquired in the equatorial (left) and polar (right) coronal regions. Left panel: proton outflow speeds measured in equatorial streamers by Susino et al. (2008) (vertical solid blue lines), Dolei et al. (2015) (vertical dotted purple lines), Spadaro et al. (2007) (vertical dashed red lines), and theoretical curves given by Morgan et al. (2008) (dashed orange curve) and by Ofman et al. (2013) (dot-dashed green curve). Right panel: proton outflow speeds measured above polar coronal holes by Strachan et al. (1993) (vertical solid blue lines), Antonucci et al. (2000) (vertical solid purple lines), Teriaca et al. (2003) (vertical dotted red lines), Dolei et al. (2016) (vertical solid green lines), Zangrilli et al. (2002) (triangle symbols), and theoretical curves given by Cranmer et al. (1999) (dashed orange curves).

speeds measured with UVCS data in both polar and equatorial regions (together with some theoretical curves) is provided in Figure 1. This figure shows that the Doppler dimming technique was successfully employed to measure proton outflow speeds between ∼20 and ∼300 km s^{-1} even if speeds below ∼100 km s^{-1} are more uncertain, as first pointed out by Strachan et al. (1993). In any case, these speeds were measured only in the altitude interval between ∼1.5 and ∼5 $R_\odot$, hence missing again the inner acceleration region where UV coronal spectra are affected by instrumental stray light owing to the stronger disk emission. Results show that in equatorial coronal streamers the wind speed is usually below the detection limit of ∼20 km s^{-1} (Noci & Gavryuseva 2007) for heliocentric distances lower than ∼3 $R_\odot$ considering both protons (Figure 1, left panel) and heavy ions (see, e.g., Strachan et al. 2002; Spadaro et al. 2007). The UVCS measurements also demonstrate that in polar coronal holes at the heliocentric distance of 1.5 $R_\odot$ the outflow speed can reach ∼50 km s^{-1} for protons (Figure 1, right panel) and ∼150 km s^{-1} for heavy ions (Antonucci et al. 2000; Zangrilli et al. 2002).

In the past, radial profiles of the outflow speed were also derived with a fourth technique from density radial profiles, by assuming mass flux conservation and a geometry for the super-radial expansion of flux tubes, hence a geometry for the underlying magnetic fields (e.g., Sittler & Guhathakurta 1999; Cranmer & van Ballegooijen 2005), even if these cannot be really considered as direct measurements of solar wind speed, but only indirect determinations. All these techniques were applied to off-limb observations of both coronal streamers (usually considered the slow wind acceleration regions) and coronal holes (where the fast solar wind originates). In particular, while the source regions of fast wind are quite well identified (see recent review by Poletto 2015), the origin of the slow wind is much more debated, because of significant magnetic complexity of the associated source regions that could be identified with streamer boundaries, stalks, cusps, and/or other regions (see the recent review by Abbo et al. 2016). Overall, the above summary points out the actual existence of a coronal region located between ∼1.1 $R_\odot$ and ∼1.5–2.0 $R_\odot$, where the solar wind outflow velocities are mainly unexplored so far.

Outflow velocity measurements of the nascent solar wind were also derived at the base of the solar corona (i.e., below ∼1.15 $R_\odot$) with XUV–EUV spectroscopic observations, by measuring line profile Doppler shifts and line asymmetries observed in coronal features (holes and active region boundaries) located on-disk. The observations of Doppler line shifts in coronal holes demonstrated the existence of 5–20 km s^{-1} outflows from the base of the corona, channeled higher up along rapidly expanding flux tubes or coronal funnels (Tu et al. 2005). These

measurements were obtained in particular with the SUMER spectrometer on board *SOHO* (e.g., Teriaca et al. 2003) and more recently with the EIS spectrometer on board *Hinode* (e.g., Fu et al. 2014) and were aimed at measuring the amount of stationary outflows occurring from the base of the corona from the plumes and interplume regions. Interestingly, significant outflow speeds (up to 60–100 km s^{-1}) were found by some authors very close to the solar limb already around 1.05 $R_\odot$ (see Patsourakos & Vial 2000; Gabriel et al. 2003). New data acquired by the most recent space-based missions have shown that the solar corona is much more complex and dynamic than previously thought, with many small-scale phenomena occurring at different frequencies (see, e.g., review by Aschwanden et al. 2001). More recently, the availability of higher-cadence observations acquired by XRT on board *Hinode* and by AIA telescopes on board *SDO* shifted the emphasis of the current research more on episodic small-scale eruptive events like polar jets. In particular, it has been suggested that polar jets, originally discovered with *Yohkoh* observations (see Shimojo & Shibata 2000) and then studied in more detail with *Hinode*/XRT (see Cirtain et al. 2007), could significantly contribute to the fast wind flow. These jets are observed in coronal holes, are associated with significant outflows (70–180 km s^{-1}; Tian et al. 2011b) already at the base of the corona, and are often associated with outflows observed higher up in VL coronagraphic images (Paraschiv et al. 2010). For this reason, it was recently pointed out that polar "jets can be used to determine the dynamical properties of the polar wind itself in the immediate vicinity of the Sun" (see recent review by Raouafi et al. 2016).

At the same time, the occurrence of frequent small-scale outflows has been observed as well at the boundaries of active regions and interpreted as a possible component of the slow wind. These outflows can reach up to 50 km s^{-1} at the base of the corona (e.g., Sakao et al. 2007; Del Zanna 2008), but a secondary component also exists that is expanding at higher velocities up to ~100–200 km s^{-1} (Hara et al. 2008; Tian et al. 2011a). This outflow from active region edges "most likely forms part of the slow solar wind" (Harra et al. 2008). Many attempts were performed to relate active region outflows with wind speeds measured in the intermediate corona (based on magnetic field extrapolations; Zangrilli & Poletto 2016) and with those measured at 1 au with in situ data (based on the distribution of elemental abundances; Brooks & Warren 2011; Culhane et al. 2014), similarly to previous attempts made during *SOHO-Ulysses* quadratures (e.g., Bemporad et al. 2003; Parenti et al. 2003). Most recently, Brooks et al. (2015) concluded (from comparison between elemental abundances in the low corona derived with EIS and in situ abundances measured by ACE) that "active region outflows appear to be the primary source" of slow wind. Nevertheless, a clear connection between active region outflows at the base of the corona and slow wind flow in the intermediate corona is missing so far. Other small-scale events that could contribute to the solar wind flows have also been identified in the chromosphere, such as the type II spicules (de Pontieu et al. 2007) and frequent small-scale chromospheric jets (discovered by the new *IRIS* mission) that "are likely to be an intermittent but continual source of mass and energy for the solar wind" (Tian et al. 2014).

The above summary showed that many authors are currently looking for possible connections between small-scale flows observed at the base of the corona with EUV disk imagers and spectrometers and large-scale bulk flows observed in the intermediate corona with VL and UV coronagraphs, or even in the interplanetary space with in situ instruments. At the same time, it is evident that an inconsistency exists between these high speeds recently inferred at the base of the corona for both coronal holes and active regions and the flows measured higher up in the intermediate corona with UV and VL coronagraphs. This actual inconsistency is more evident for the association between the speed of active region outflows from the base of the corona and the almost negligible outflows measured higher up around 2.5–4.5 $R_\odot$ in coronal streamers with both UV spectroscopy and VL blob tracking. On the other hand, the same inconsistency seems also to exist for the association between polar jet outflows and the outflow speeds measured higher up, if the jets are significantly contributing to the solar wind flow. Hence, the aim of this paper is to propose a possible connection between outflows sampled on-disk at the base of the corona and outflows measured off-limb in the intermediate corona. The idea proposed here is the possible existence of a quasi-stagnation point of the solar wind located in this unexplored region where the solar wind speed could reach a minimum value, being further reaccelerated higher up. This possibility is supported here with the combined analysis of UV and VL coronagraphic data. The paper is structured as follows: after a description of the data analyzed here and of the observational results (Section 2), assumptions and uncertainties on the results are discussed (Section 3), a possible theoretical interpretation for results is provided (Section 4), and then the results are summarized and discussed (Section 5).

2. Observations and Data Analysis

The observational part of this work is based on a combined analysis of VL and UV coronagraphic data. The main idea can be summarized as follows: solar wind outflow speeds are derived here by using the Doppler dimming technique and extending this technique to inner coronal regions that have never been explored so far. To this end, it is necessary to have coronagraphic images in both VL and UV wavelength ranges covering continuously a broad interval of heliocentric distances starting very close to the Sun (possibly down to 1 $R_\odot$). Because no single instrument is able to cover such a broad altitude interval, it is necessary to interpolate and extrapolate the observed intensities at missing regions, as is explained below in more detail. For reasons that are explained below, no more than one single UV image per day can be built; hence, to increase the statistical significance of the analysis performed here, the same analysis has been applied over many days of coronagraphic observations. The time interval has been selected focusing around the minimum of the 23rd solar activity cycle in order to have a simpler distribution of coronal structures (broad equatorial streamers and extended polar coronal holes) associated with an almost dipolar global magnetic field configuration. Moreover, for the analysis performed here it is necessary to have for the same day at least one VL polarized brightness (pB) image and a full sequence of UV observations covering the whole inner corona. After a search on the data catalogs, the best period matching these requirements turns out to be in 1997 June. In the next paragraphs I explain how these data have been combined and analyzed.

2.1. Interpolated VL Coronagraphic Images

The interpolated VL images have been built by combining images acquired with two different instruments: the space-based *SOHO* LASCO-C2 coronagraph and the ground-based Mauna Loa Sola Observatory (MLSO) MK3 coronagraph. For the purposes of this work, it is necessary to build an interpolated image of the VL *pB* extending from the base of the corona out to at least 6 $R_\odot$. The MLSO MK3 instrument provided daily *pB* images with a good signal-to-noise ratio from 1 $R_\odot$ up to about ∼1.5 $R_\odot$, while the LASCO-C2 *pB* daily images extend from ∼2.1 $R_\odot$ out to 6.0 $R_\odot$. In this work, in order to avoid the region affected by the diffraction pattern very close to the inner occulter edge, the LASCO-C2 data have been analyzed starting from the projected altitude of 2.5 $R_\odot$; for similar reasons the MLSO data acquired below 1.1 $R_\odot$ have not been considered. Moreover, MLSO data acquired above 1.5 $R_\odot$ were also excluded, to avoid coronal regions with lower signal-to-noise ratio. The MLSO MK3 data are provided as calibrated *pB* images, while the LASCO-C2 *pB* images have been calibrated by using the standard procedures distributed to the community within *SolarSoftware*. The data gap between ∼1.5 and ∼2.5 $R_\odot$ can be filled quite easily by performing radial power-law fittings of the *pB* measured by the two instruments and by replacing the missing values with the resulting fitting function. In particular, in this work the radial profiles of $pB(r)$ values have been fitted with a double-power-law function $I(r)$ with general expression $I(r) = A\ r^{-B} + C\ r^{-D}$. Once the four free parameters are determined from the fit, the same function can thus be used to extrapolate the *pB* intensity down to the base of the corona between 1.1 and 1.0 $R_\odot$. Figure 2 shows an example of a combined MLSO plus *SOHO* original *pB* images (top left panel) and the resulting interpolated image (top right panel) for one of the days analyzed here. With this technique the reconstructed VL images have also been cleaned for stars, cosmic rays, and missing blocks. The data interpolation and extrapolation have been applied to all the data available in 1997 June; unfortunately, during this 30-day-long period there are 13 days of missing MLSO data, specifically for June 4, and for all the days between June 19 and 30. Hence, in what follows these days have not been considered in the combined VL and UV data analysis, in order to avoid any possible additional uncertainty related to the extrapolation of the *pB* intensity below ∼2.5 $R_\odot$ when no MLSO data were available.

2.2. Interpolated UV Coronagraphic Images

As mentioned in the Introduction, the outflow velocities have been determined here by using the Doppler dimming technique, hence by taking advantage of the coronal spectral lines whose emission is partially or entirely due to the radiative excitation (followed by spontaneous emission) by chromospheric photons emitted in the same line. This component of the line is usually referred to as the radiative component, to make a distinction with the second most prominent process responsible for EUV–UV emissions, which is the collisional excitation due to collisions with coronal electrons, producing (after spontaneous emission) the so-called collisional component. If the scattering atom is moving with respect to the atom emitting the exciting radiation, then the atomic absorption profile is Doppler-shifted with respect to the emission profile, thus reducing the efficiency in the excitation process and leading to a dimming in the intensity of the coronal plasma emission in that line. By measuring this dimming, the flow speed of the scattering atom can be determined. This is the principle of the Doppler dimming technique.

In this work the outflow velocities have been determined by using the brighter emission line of the UV spectrum: the H I Lyα λ1215.67 spectral line (hereafter Lyα), which in coronal plasma conditions is almost entirely due to radiative excitation. The determination of the velocities is described in the next section. For the purposes of this work, it was necessary to build continuous 2D images of the coronal Lyα emission from 1 $R_\odot$ out to 6 $R_\odot$. To this end, it is possible to use the so-called UVCS synoptic observations that were acquired daily besides the special observation programs. The instantaneous field of view (FOV) of the UVCS slit was a 40′ long straight line placed off-limb always tangent to the solar limb; during operations, it was possible to change the slit central latitude, rotating it around an axis pointing toward the Sun's center in order to cover different coronal regions, and to move it at different projected heliocentric distances in a range between 1.4 and 10 $R_\odot$. During the synoptic observations, the full corona was scanned with the slit spectrometer covering different altitudes and centered at eight different latitudes at steps of 45°, as shown in Figure 2 (bottom left panel). More specifically, each synoptic sequence is made of spectra acquired with the slit centered at projected altitudes of 1.42, 1.67, 1.90, 2.34, 2.68, and 3.11 $R_\odot$ above the equatorial east and west limbs, at 1.42, 1.71, 2.00, 2.28, and 2.56 $R_\odot$ above the polar north and south limbs, and at 1.42, 1.71, 2.00, and 2.28 $R_\odot$ at intermediate latitudes. All data were acquired with a slit width of 500 μm and exposure times of 100 s, with the exception of polar spectra, which were acquired with 300 s exposure times.

As a first step, for each position of the spectrometer slit the Lyα intensity was derived with Gaussian fitting of the line profiles, thus producing a discontinuous distribution of the line intensity in the corona (bottom left panel of Figure 2). Then, in order to cover the missing coronal regions, it is necessary to interpolate and extrapolate the intensities by using the observed values. To this end, similarly to what was already described for the VL data, the 2D discontinuous image was analyzed along radial directions by extracting at each angle in the latitudinal iteration all the available Lyα intensities, by fitting them with a double-power-law function $I(r) = A\ r^{-B} + C\ r^{-D}$, and by replacing the input values with the output fitting values. Typically for each power-law fitting from a minimum of 5 up to a maximum of 8 data points were available at different altitudes, depending on the considered latitude. In this way, a 2D Lyα continuous image was produced covering the whole interval of heliocentric distances between 1 and 6 $R_\odot$. Figure 2 shows an example of an original *SOHO* UVCS Lyα synoptic image (bottom left panel) and the resulting interpolated and extrapolated image (bottom right panel) for one of the 30 days analyzed here.

For the purposes of this work it is very important to point out here that in the output 2D images the UV intensities above 3.1 $R_\odot$ in the equatorial region and above 2.6 $R_\odot$ in the polar region, as well as those at all latitudes and distances below 1.42 $R_\odot$, are based only on extrapolations of the measured intensities; on the other hand, the UV intensities in the intervals between 1.42 and 3.0 $R_\odot$ around the equator and between 1.42 and 2.5 $R_\odot$ around the poles are based on interpolations of the observed values. With this technique none of the coronal complexity at low heights (due to small-scale

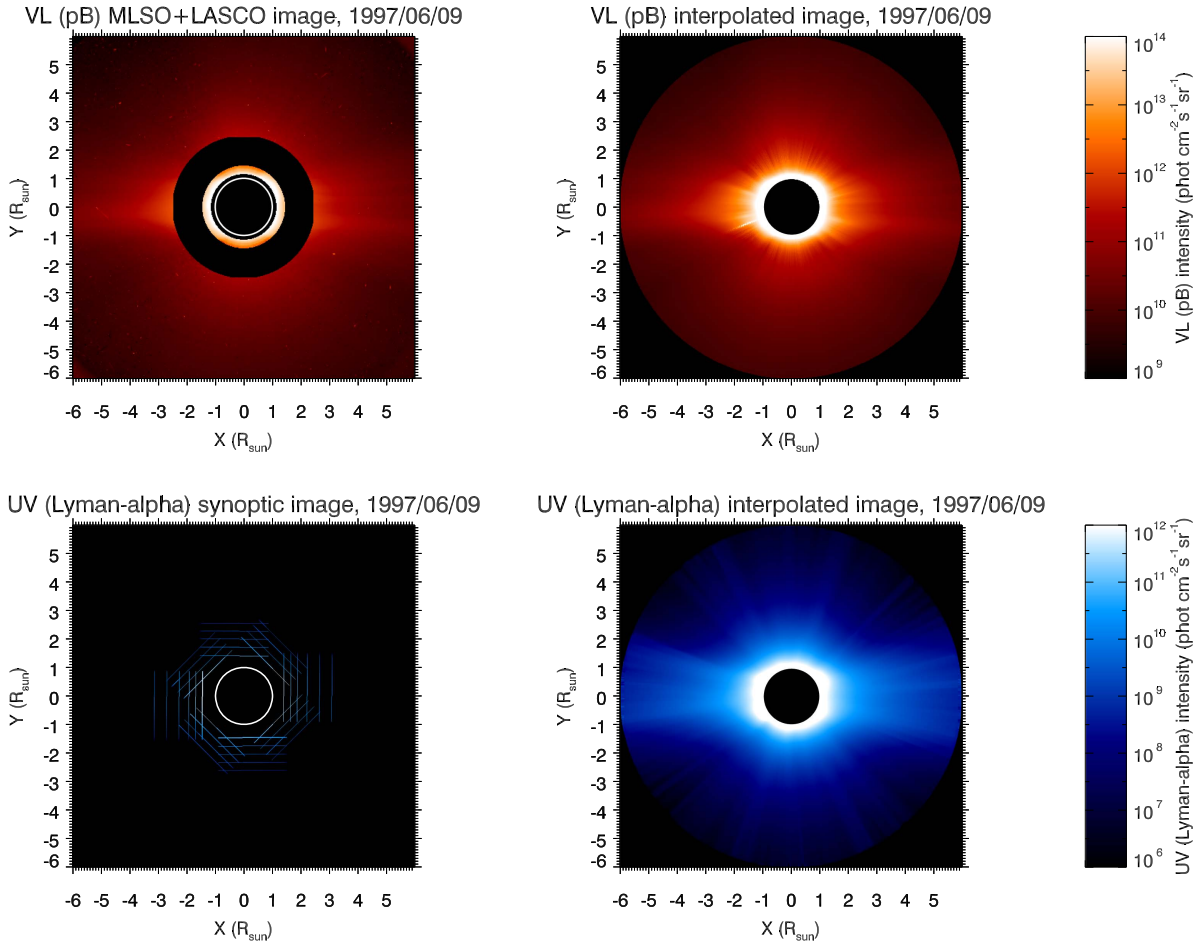

Figure 2. Top: example of a combined MLSO/MK3 (inner part) and *SOHO*/LASCO-C2 (outer part) coronal *pB* image (left) and the reconstructed (interpolated) full *pB* image (right). Bottom: example of a UVCS synoptic observation sequence in the H I Lyα line (left) and the corresponding reconstructed (interpolated and extrapolated) full Lyα image. All these images are shown for one of the 30 days of observations analyzed in this work (an animation showing the whole month of 1997 June is available online).

(An animation of this figure is available.)

features like coronal loops, plumes, etc.) will be reproduced by an extrapolation from the higher heights; the extrapolation will reproduce only the Lyα intensity decay of large-scale features (such as coronal streamers and coronal holes), which is expected to follow at all altitudes a power-law decay, as recently shown, for instance, by Vial & Chane-Yook (2016). In any case, the intensities in the extrapolated regions are expected to have larger uncertainties with respect to intensities in the interpolated regions.

2.3. Determination of the Outflow Speed Images

Once a series of daily 2D VL (*pB*) and UV (Lyα) images are built, the analysis for the determination of the outflow speed has been applied. In particular, in this work the outflow speed has been determined based on the technique originally described by Withbroe et al. (1982) and suggested by G. Noci. In particular, in first approximation the intensity of the radiative component I_r of a spectral line can be written as the following integral along the line of sight (LOS):

$$I_r = K_r \times \int_{\rm LOS} A_{\rm el}\, R_i(T_e) n_e\, \bar{J}\, dz \qquad (1)$$

where K_r is a constant parameter,

$$\bar{J} = \int_{-\infty}^{+\infty} J(\lambda)\phi(\lambda - \lambda_w) d\lambda, \qquad (2)$$

$A_{\rm el}$ is the elemental abundance (relative to hydrogen) for the considered emitting ion, $R_i(T_e)$ is the ionization fraction (dependent on the electron temperature T_e), n_e is the electron density, $J(\lambda)$ is the intensity of the disk radiation at wavelength λ, $\phi(\lambda)$ is the ion absorption profile, and $\lambda_w = \lambda_0(1 + \boldsymbol{v}\cdot\boldsymbol{n}/c)$ is the Doppler shift induced by the solar wind velocity $\boldsymbol{v}$ multiplied by the vector $\boldsymbol{n}$ describing the direction of the incoming exciting photon. Under the hypothesis that no significant variation of the elemental abundance $A_{\rm el}$ and electron temperature (and hence of ionization fraction R_i) occurs along the LOS, the above expression can be rewritten as

$$I_r \propto A_{\rm el}\, R_i\, \langle D_i(v_w)\rangle \int_{\rm LOS} n_e\, dz, \qquad (3)$$

where v_w is the radial component of the wind speed and D_i is the Doppler dimming term ($0 \leqslant D_i \leqslant 1$, with $D_i = 1$ for $v_w = 0$ and $D_i \longrightarrow 0$ for $v_w \longrightarrow \infty$).

On the other hand, the intensity $I_{\rm VL}$ of the VL corona (*pB*) due to Thomson scattering by coronal electrons of the disk

radiation can be written again as an integral along the LOS:

$$I_{\rm VL} = K_{\rm VL} \times \int_{\rm LOS} n_e \, \bar{J} \, dz, \quad (4)$$

where $K_{\rm VL}$ is a constant quantity. Hence, the ratio $I_r/I_{\rm VL}$ between these two intensities is mainly dependent on the Doppler dimming coefficient:

$$I_r/I_{\rm VL} = K \times \langle D_i(v_w) \rangle, \quad (5)$$

with K a constant quantity; this means that from the observed ratio the Doppler dimming coefficient D_i can be measured, and thus the wind speed v_w.

The important advantage of this technique is that the electron density distribution n_e, which is the quantity undergoing major variations along the LOS, is simplified in the ratio. Hence, the wind speed can be measured independently on the unknown density profile $n_e(z)$ along the LOS. Moreover, given a couple of UV and VL images acquired at the same time from the same point of view, the above technique allows one to easily convert the intensity ratio image into a 2D Doppler dimming image, and hence a 2D outflow speed image. This makes this technique very interesting for the future analysis of data that will be provided by the Metis coronagraph on board *Solar Orbiter* (Antonucci et al. 2012; Fineschi et al. 2012). Nevertheless, it is important to point out that for the Lyα line there is an upper limit speed that can be measured; in fact, for outflow velocities larger than $\sim$500 km s^{-1} the Doppler dimming coefficient $D_i(v_w \sim 500 \text{ km s}^{-1}) \simeq 0$ and the inversion cannot be performed anymore. It is also important to point out here that speeds measured with this technique are relative only to neutral hydrogen atoms, and hence coronal protons (as far as the two species share the same speed), and thus will be different, for instance, from those derived by UVCS for heavy ions (specifically O^{5+} ions).

Independently from the derivation of the outflow speed v_w, the electron density 2D maps have been derived here from the analysis of VL coronagraphic images acquired in 1997 June. In particular, once calibrated VL (pB) images are provided, the electron density n_e on the plane of the sky is derived by the standard van de Hulst inversion technique (van de Hulst 1950), which simply assumes cylindrical symmetry of the whole corona. Results for v_w and n_e distributions are discussed in the next section.

3. Discussion of Results

The determination of the outflow speed maps requires a series of assumptions that are briefly discussed here. First, it is necessary to assume not only that electron temperatures T_e are not changing significantly along the LOS but also a T_e distribution on the plane of the sky; in the above equations the hypothesis of T_e affects the fraction of neutral hydrogen atoms $R_{\rm H}(T_e)$. Second, it is necessary to assume the shape of the exciting radiation profile $J(\lambda)$ and to assume that this profile is not changing along the LOS (hence neglecting possible features on the solar disk such as active regions, quite Sun, and coronal hole regions); in the above equation this parameter affects the relationship between the wind speed v_w and the Doppler dimming coefficient D, allowing the derivation of $v_w = D^{-1}[I_r/(K\ I_{\rm VL})]$. Third, it is also necessary to assume a shape for the atomic absorption profile $\phi(\lambda)$ (related to the proton kinetic temperature T_k) and to assume that this profile is not changing significantly along the LOS (hence neglecting temperature anisotropies); this parameter is also affecting the function $D_i(v_w)$ to be inverted to derive v_w. These assumptions are then discussed here.

First, the assumption of T_e corresponds to assuming the plane-of-sky distribution for the fraction of neutral hydrogen atoms R_H in the corona. As was first pointed out by Withbroe et al. (1982), the collisional ionization time for neutral hydrogen becomes larger than the coronal expansion time above $r \sim 8\ R_\odot$ in equatorial regions and above $r \sim 3\ R_\odot$ in coronal holes. Hence, below these altitudes a radial variation of R_H is expected, while above these altitudes the fraction of neutral hydrogen atoms will "freeze-in" and R_H will be almost constant with altitude. The radial variation of T_e and thus R_H is in general unknown: in this work it is assumed that $T_e(r)$ is at all latitudes given by an average between the temperature profiles provided by Vásquez et al. (2003) for the equatorial and the polar regions. According to the Vásquez et al. (2003) profiles, the expected difference in the values of R_i between the polar and equatorial regions is increasing with altitude and is reaching a maximum value of $\sim$40% at the outer edge of the considered range ($r = 6\ R_\odot$). As was verified here, an uncertainty by $\pm$40% in the R_H value implies an uncertainty by $\pm$10% in the computation of the output values of v_w with the method explained above.

Second, in this work the shape of the exciting Lyα profile has been assumed from on-disk measurements by SUMER provided by Lemaire et al. (2002), with total disk intensity $I_{\rm disk}({\rm Ly}\alpha)$ assumed from the average of measurements acquired by the *Solstice* satellite on 1997 June equal to $I_{\rm disk}({\rm Ly}\alpha) = 5.35 \cdot 10^{15}$ photons cm^{-2} s^{-1} sr^{-1}. As usual, the disk intensity exciting the H atoms at altitude h has been diluted with altitude by taking into account the variation of the solid angles $\Omega_{\rm AR}$ and $\Omega_{\rm sun}$ subtended, respectively, by active regions and by the whole solar disk, by assuming 5% of the solar surface to be covered by active regions to reproduce the total intensity measured by *Solstice*. It was verified here that an increase (decrease) even by a factor of 2 in the total Lyα disk intensity (larger than the Lyα disk intensity variations usually observed along the whole solar cycle) would imply an increase (decrease) only by $\sim$20% in the derived values of v_w.

Third, the atomic absorption profile has been assumed equal to a Gaussian profile with $\sigma = 0.37$Å corresponding to $T_k = 10^6$ K at all latitudes and heliocentric distances. This assumption is not in agreement with the results obtained by many different authors and based on the analysis of UVCS data showing that the proton kinetic temperatures T_k change with the projected altitudes and latitudes in the corona, and that protons have a temperature anisotropy, with kinetic temperatures $T_{k\perp}$ perpendicular to the magnetic field being larger than temperatures $T_{k\parallel}$ parallel to the magnetic field, in particular in coronal holes (see review by Kohl et al. 2006, and references therein). Nevertheless, measurements of T_k from the observed Lyα line widths are quite uncertain, first because the measured line widths need to be corrected for the unknown nonthermal plasma motions (due, e.g., to propagating plasma waves) and for the UVCS instrumental effects (such as line broadening, but also other effects; see Kohl et al. 1997). A second source of uncertainty is the possible contamination of the coronal line profile by other sources of Lyα emission, such as the interplanetary emission (see, e.g., Suleiman et al. 1999) and the scattered chromospheric emission (see, e.g., Cranmer et al. 2010). Moreover, some authors pointed out that the possible

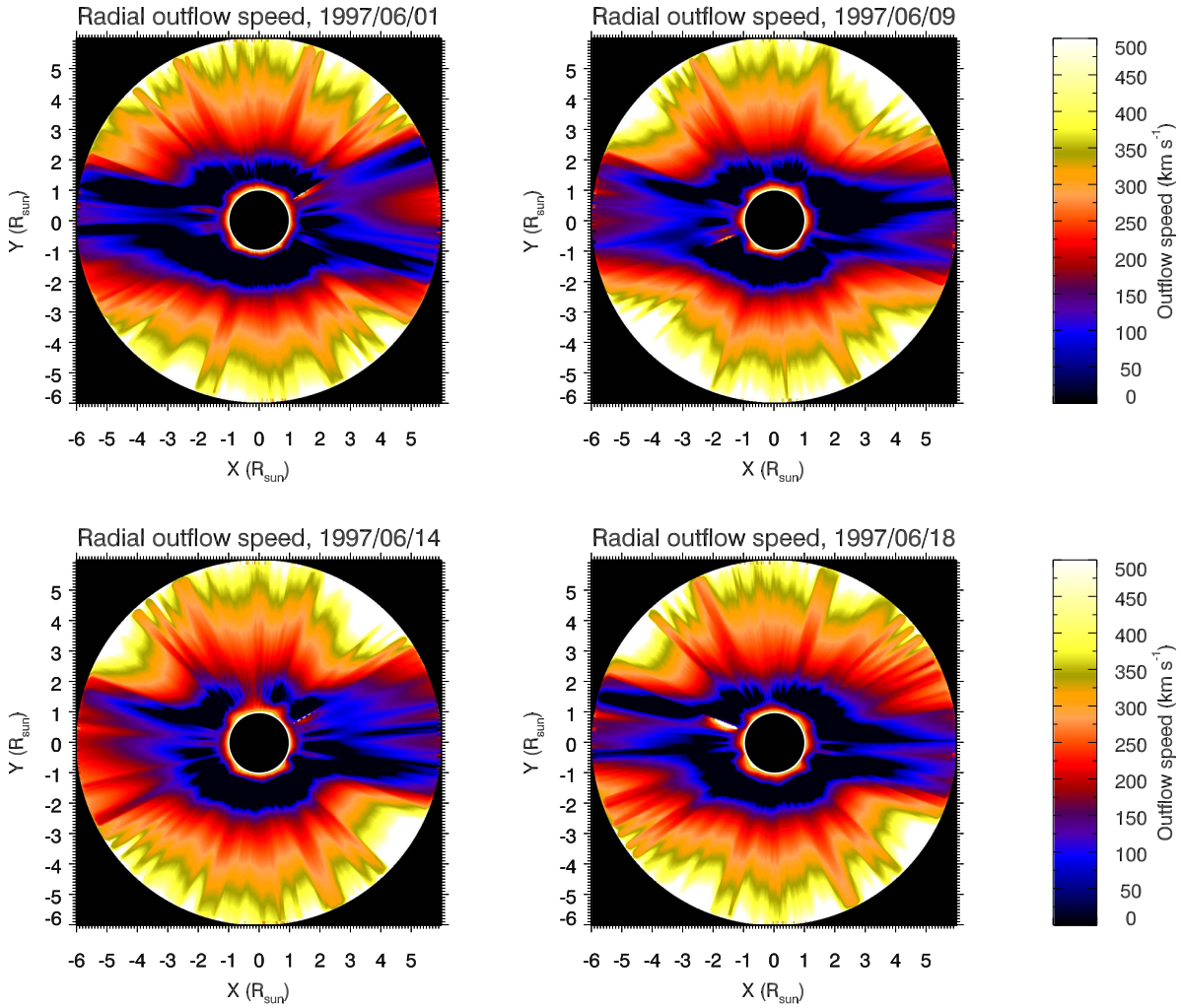

Figure 3. Sequence of radial outflow velocity images as derived from the ratio between VL and UV coronal emissions over four different days of 1997 June (an animation showing the whole month of 1997 June is available online). The outer white region corresponds to altitudes where the Doppler dimming technique with Lyα spectral line cannot be applied anymore (see text).

(An animation of this figure is available.)

effects of Lyα line broadening due to integration along the LOS could not be correctly constrained for both coronal holes (Raouafi & Solanki 2006) and coronal streamers (Labrosse et al. 2006).

All these sources of uncertainty result in a large spread on the possible values of the proton kinetic temperatures T_k provided in the literature (see, e.g., Kohl et al. 2006, Figure 39, dotted blue lines). For these reasons, and in order to avoid any possible additional bias on the results presented here introduced by assuming different coronal distributions of $T_{k\perp}$ and $T_{k\parallel}$, in this work a simple constant and isotropic kinetic temperature $T_{k\perp} = T_{k\parallel} = 10^6$ K was assumed at all latitudes and heliocentric distances. The assumption of temperature isotropy is more realistic for coronal streamers (e.g., Spadaro et al. 2007), but not realistic for coronal holes (e.g., Cranmer et al. 1999). In any case, as was verified here by repeating the analysis for different values of T_k, an increase (decrease) by a factor of 2 in the proton kinetic temperature would imply a decrease (increase) only by $\sim$10% in the derived values of v_w. Moreover, the fact that the derived proton v_w values have a quite weak dependence on the assumed T_k anisotropy has been recently demonstrated by the statistical analysis performed by Dolei et al. (2016). In particular, a comparison between proton outflow speed values provided by these authors under the two opposite assumptions of temperature isotropy or maximum temperature anisotropy (their Table 2) shows differences on the order of only 6%–12%, with velocities derived under the isotropic assumption being systematically higher.

Summing in quadrature all the possible sources of uncertainty listed above, the resulting total uncertainty on the proton speed values derived in the interpolated regions is expected to be not larger than $\simeq$25%, while larger uncertainties will affect the regions where the UV Lyα emission was extrapolated. These uncertainties are comparable to those estimated, for instance, by Strachan et al. (1993) based on measurements acquired with sounding rocket flights before the launch of *SOHO*. Considering all these uncertainties, the 2D outflow speed images derived for four different days of 1997 July are shown as an example in Figure 3 (a movie for the full period is available online). The first thing to notice in these images is that there is a clear difference between the equatorial regions, where the slow wind speed never exceeds $v_w \simeq 200$ km s^{-1} up to 6 $R_\odot$, and the polar regions,

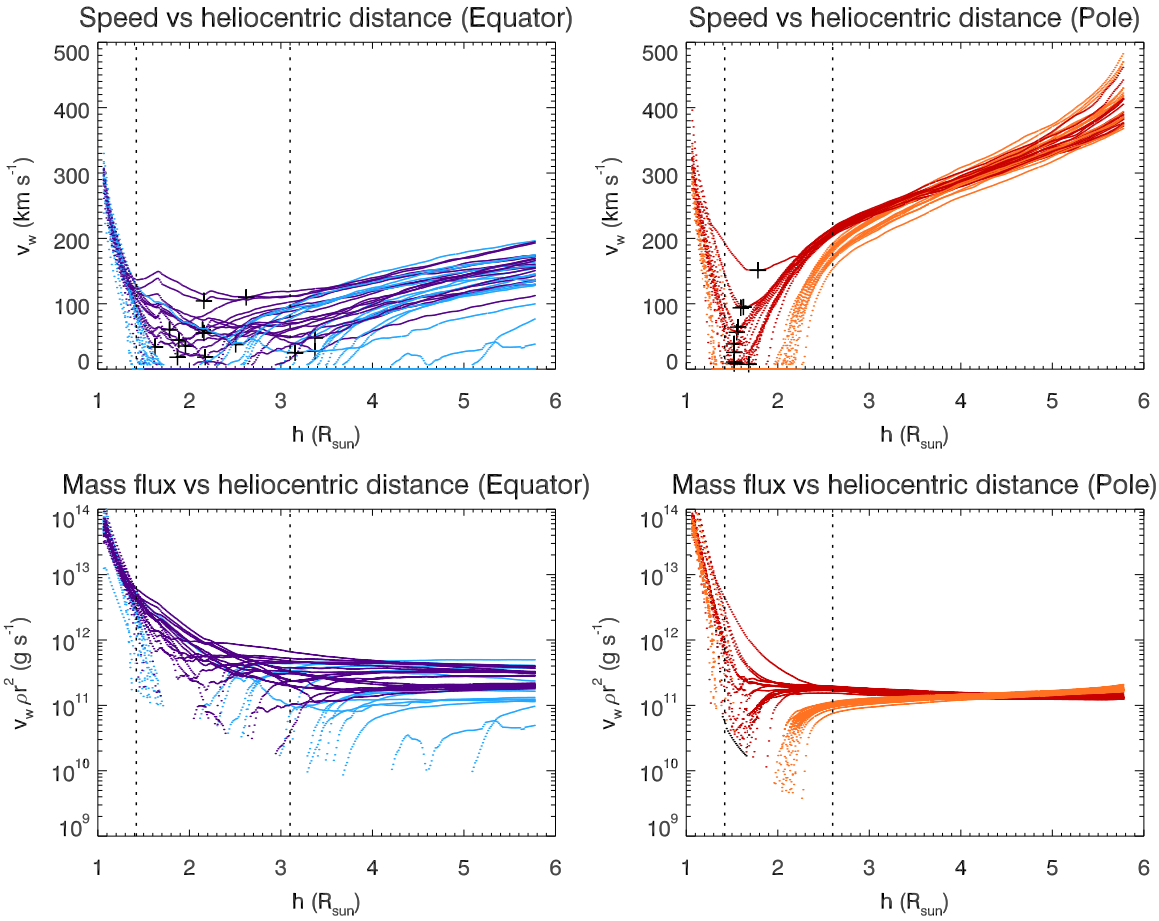

Figure 4. Top: scatter plots of radial profiles of speeds derived for different days of 1997 June in the equatorial regions above the west (light blue) and east (purple) solar limbs (left) and in the polar regions above the north (dark red) and south (orange) solar limbs (right). Bottom: scatter plots of radial profiles of solar wind mass flux in the equatorial regions above the west (light blue) and east (purple) solar limbs (left) and in polar regions above the north (dark red) and south (orange) solar limbs (right). In all panels the vertical dotted lines mark the minimum and maximum distances where UVCS observations were acquired; out of this interval the UV Lyα intensities were extrapolated. Plus signs in the top panels show the positions of local minima of proton outflow speed profiles.

where the fast wind speed reaches quickly the saturation value of $v_w \simeq 500$ km s^{-1} around 6 $R_\odot$. This is in agreement with the expected latitudinal distribution of slow and fast wind components. The time evolution also shows that the equatorial regions are characterized by nearby wind streams with different outflow velocities changing latitudinal location day by day, while in the polar regions there are different streams, but their latitudinal distribution is more stable with time.

Other interesting properties are better shown in the top panels of Figure 4, showing radial equatorial and polar plots of the inferred speeds for different days on 1997 June. First, the top left panel of Figure 4 shows no significant differences between the equatorial velocity radial profiles measured above the west (light-blue points) and east (purple points) solar limbs. On the contrary, the top right panel of Figure 4 shows a clear asymmetry between the fast wind velocities measured over the two poles, with the velocities above the south pole (orange points) being systematically lower than those measured above the north pole (dark red points) closer to the Sun (i.e., below $\sim$3 $R_\odot$). This is very interesting, because it is well known that the whole solar activity has north–south asymmetries (see discussion). On the other hand, the top panels of Figure 4 also show a much larger variability of the slow wind speeds at higher altitudes with respect to fast wind speeds; this is in agreement with in situ data showing that fast solar wind is extremely uniform with respect to slow solar wind, whose speed is more discontinuous (e.g., McComas et al. 2000). Overall, values shown in these panels are also in very nice agreement with proton outflow speeds measured by previous authors for both equatorial and polar regions (see Figure 1).

Derived outflow speeds v_w can be also combined with plasma mass densities $\rho = n_e \mu_e m_{\rm H}$ (where $m_{\rm H}$ is the mass of hydrogen atoms, $\mu_e = (1 + 4\alpha)/(1 + 2\alpha) \simeq 1.18$ is the mean molecular mass per electron, and $\alpha = n_\alpha/n_p \simeq 0.11$ is the He abundance) to measure the solar wind mass flux $F_w = v_w \rho\, r^2 f_w$, with an $f_w \geqslant 1$ flux tube expansion factor and $A(r) = f_w(r) r^2$ cross-sectional area of the flux tube (Wang & Sheeley 1990). The mass flux F_w has been computed here by simply assuming $f_w = 1$ everywhere; hence, because the conservation of mass flux implies that $F_w =$ const. everywhere with altitude, regions where F_w decreases represent corresponding increases in the expansion factor f_w. This quantity is thus very interesting, because radial profiles of F_w allow one to identify the coronal regions where F_w is constant (and hence the plasma is expanding almost radially) and those where F_w is not constant (and hence super-radial expansion is occurring).

Resulting radial profiles of F_w are shown in the bottom panels of Figure 4 for both the equatorial (bottom left) and polar (bottom right) regions; values obtained at higher altitudes in these plots

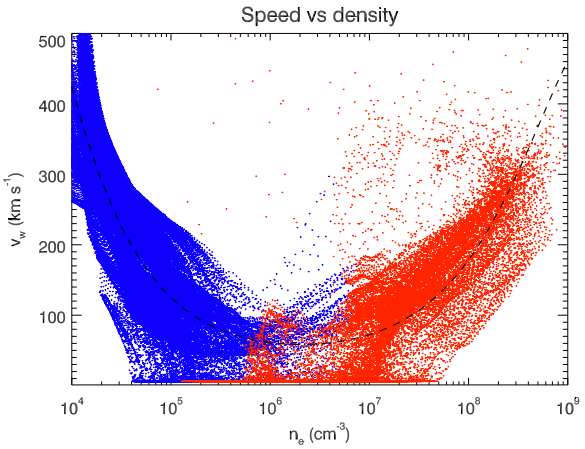

Figure 5. Scatter plot of densities vs. outflow speeds measured on 1997 June 9, for heliocentric distances between 1.0 and 1.8 $R_\odot$ (red points) and between 1.8 and 6.0 $R_\odot$ (blue points). The black dashed line shows a fourth-order polynomial fitting (see text).

are in agreement with the proton mass fluxes measured with in situ data by ACE at 1 au, which are on average in the range of $v_w n \sim 2 \cdot 10^8$–$4 \cdot 10^8$ cm^{-2} s^{-1}, corresponding to $F_w \sim 7.5 \cdot 10^{10}$–$1.5 \cdot 10^{11}$ g s^{-1} (see Wang 2010, and references therein). Plots in the bottom panels of Figure 4 indicate that the slow wind has a significant variability of F_w values and reaches a constant value in a quite broad interval of heliocentric distances between ~2 and ~3.5 $R_\odot$, independently of the considered solar limb. On the other hand, the fast solar wind reaches an almost constant mass flux much closer to the Sun and in a shorter interval of heliocentric distances between ~1.5 and ~2.5 $R_\odot$. This means that significant super-radial expansions occur below these intervals for both equatorial and polar regions. Quite interestingly, the polar regions show much more uniform mass flux with respect to equatorial regions, as expected, but also slightly different radial profiles of F_w from north to south. In particular, while in the north pole F_w reaches larger and almost constant values at lower distances, the south pole has lower F_w values closer to the Sun, but slowly increasing with distance up to values slightly larger than those at the north pole. This different behavior is related again to the mentioned north–south asymmetries in the solar activity.

Another very interesting result found here is the existence of a strong relationship between the plasma density and the outflow velocity. In particular, as is shown in Figure 5, in the inner corona (1.0–1.8 $R_\odot$; red points) the outflow velocity is almost correlated with the density, while higher up (1.8–6.0 $R_\odot$; blue points) the opposite occurs, with the outflow velocity almost anticorrelated with the density. This last result is in agreement again with in situ measurements demonstrating that at 1 au fast wind streams have a density lower than slow wind streams (see, e.g., Richardson et al. 2003, and references therein). This correlation at lower distances and the anticorrelation at higher distances between v_w and n_e have been fitted here with a fourth-order polynomial

$$\log_{10} v_w = \sum_{n=0}^{4} P_n (\log_{10} n_e)^n . \quad (6)$$

If the outflow speed is measured in cm s^{-1} and the electron density in cm^{-3}, the values of the five coefficients P_n resulting from the fit are $P_0 = (0.57 \pm 0.06)$, $P_1 = (6.65 \pm 0.04)$, $P_2 = (-2.02 \pm 0.01)$, $P_3 = (0.239 \pm 0.001)$, and $P_4 = (-9.62 \pm 0.06) \cdot 10^{-3}$. This fitting function (also shown in Figure 5 with a black dashed line) can be used as an empirical relationship between coronal plasma densities and outflow speeds at all latitudes. With this relationship, for instance, a 2D coronal density image can be easily converted into a 2D outflow speed image v_{wn}. Figure 6 shows as an example the comparison between the outflow speed v_w measured here from combined UV and VL image analysis and the speed v_{wn} inferred for the same day with the above empirical relationship using densities measured with VL data. This comparison shows that the radial evolution of the solar wind speed is not reproduced very well (particularly above the poles), and not even the complexity of multiple radial features visible in both the equatorial and polar regions. Nevertheless, the overall modulation of fast and slow wind regions is reproduced quite well, particularly at larger distances from the Sun, as well as the average value of the fast and slow wind speed at that altitude (bottom panel of Figure 6). Hence, the empirical relationship provided here between n_e and v_w could be really useful, for instance, to derive information on the large-scale properties of solar wind and on its evolution during different solar rotations or even solar cycles.

The most important and unexpected result shown in the previous figures (particularly in Figures 3–6) is the existence of high speeds ($v_w >$ 100 km s^{-1}) very close to the solar surface; starting from near the solar surface and moving at higher altitudes, the wind speed first decreases and then increases again after a local minimum. The location of the local minimum is around 2.0 $R_\odot$ in the equatorial regions (Figure 4, plus signs in the top left panel) and around 1.5 $R_\odot$ for the polar regions (Figure 4, plus signs in the top right panel). This radial variation of the wind speeds in the inner corona has never before been reported. For this reason, it is very important to remind the reader that the speeds in the coronal regions below the heliocentric distance of 1.42 $R_\odot$ have not been measured directly in this work, but have been inferred from the ratio between the VL (pB) intensities observed by MLSO MK3 and the UV (Lyα) intensities extrapolated back to 1 $R_\odot$ from *SOHO* UVCS observations. Hence, the possibility that this result is a consequence of the UV intensity extrapolation cannot be ruled out. In principle, it is possible that the high speeds derived here in the inner part of the corona between 1.0 and 1.42 $R_\odot$ are partially or totally an extrapolation artifact, due to a wrong estimate of the UV Lyα intensities. In fact, if the Lyα intensity below 1.42 $R_\odot$ is for any reason underestimated (overestimated), the result of the computation will be that the lower (higher) intensities are due to lower (higher) values of Doppler dimming factor D_i, and hence to higher (lower) velocities, thus providing an overestimate (underestimate) of v_w values.

On the other hand, it is also very important to point out that the local minima of the outflow speeds are located above the heliocentric distance of 1.42 $R_\odot$ (as shown in the top panels of Figure 4), and hence in the regions where the UV intensities have been interpolated and not extrapolated. In these interpolation regions the uncertainties on real UV intensities are much smaller, and the results are much more reliable.

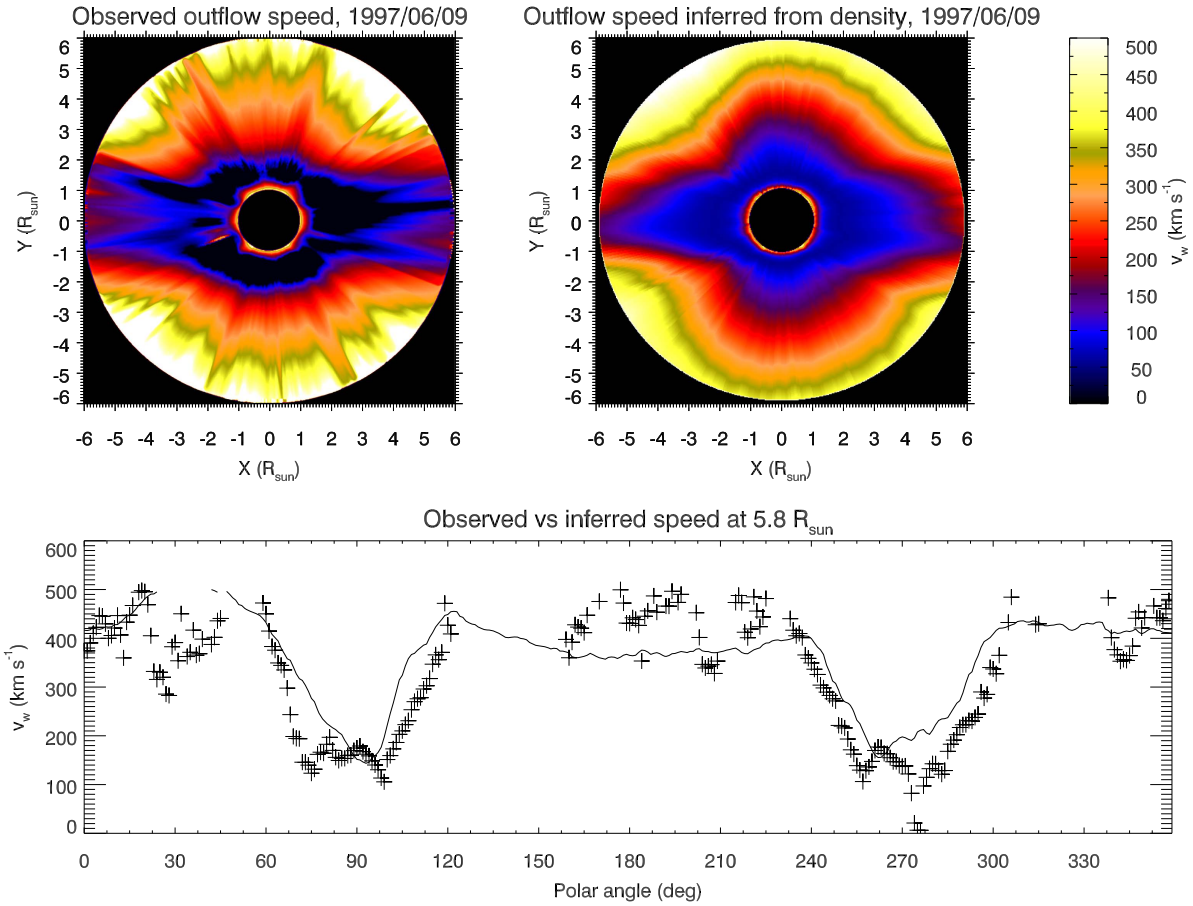

Figure 6. Top: comparison between the outflow speed v_w derived here with the combined analysis of UV and VL intensities (left) and the speed $v_{\rm wn}$ inferred directly from electron densities measured with VL images (right) by using the empirical relationship between densities and velocities (see text). Bottom: comparison between the latitudinal distribution of v_w (plus signs) and $v_{\rm wn}$ (solid line) at the constant heliocentric distance of 5.8 $R_\odot$ as a function of polar angle (measured counterclockwise from the north pole).

Hence, even if the high speed values inferred below 1.42 $R_\odot$ could be overestimated, the existence of the local minima in the outflow speed radial profiles is a much more reliable result.

Keeping this in mind, the existence of these local minima and the outflow speed profiles and of these near-Sun high speeds is very interesting because it could represent the missing "conjunction ring" between the fast flows measured at the base of the corona in active region boundaries and coronal holes (mentioned in the Introduction) and the flows measured higher up in the intermediate corona. These results could solve in particular the apparent discrepancy between former UVCS results on slow solar wind speed (very small or even negligible outflow speeds below 3 $R_\odot$ in coronal streamers) and the most recent results obtained by *Hinode*/EIS and *IRIS* showing persistent outflows with velocities up to 50 km s^{-1}or even larger from the boundaries of active regions. Hence, in what follows I try to explore from a theoretical point of view the possible existence of these near-Sun high speeds and of a quasi-stagnation region at the base of the corona.

4. Interpretation of Results

In order to investigate the possible consequences of results described above, I restart here from the classical Parker's momentum equation for a single fluid stationary solar wind, for the more general case of non-isothermal corona, by assuming spherical symmetry, and by adding an external force $f_{\rm ext}$ responsible for the solar wind acceleration:

$$\rho v\frac{dv}{dr} = -\frac{dP_{\rm gas}}{dr} - \frac{G\,M_\odot \rho}{r^2} + f_{\rm ext}\,, \qquad (7)$$

where $v(r)$ is the radial wind speed, $\rho(r)$ is the plasma mass density, and $P_{\rm gas}(r) = 2n_e k_B\,T(r) = [\rho(r)/\mu {\rm m_H}]k_B\,T(r)$ is the gas pressure given by the perfect gas law. Once 2D images for the plane-of-sky distribution of $v(r)$ and $\rho(r)$ are provided, these images can be used to derive the 2D distribution of corresponding velocity (dv/dr) and density ($d\rho/dr$) radial gradients. The derivation of 2D outflow speed images has been discussed in the previous paragraph, and it is important to remind here that the Doppler dimming technique provides an estimate of the radial component of outflow speed, thus suitable for the measurement of the radial gradient. Figure 7 shows an example of 2D distributions of the plasma density (top left) and outflow velocity (top right) and the corresponding density (bottom left) and velocity (bottom right) radial gradients for a selected day (1997 June 9) during the time interval analyzed here.

The derivation of $f_{\rm ext}$ requires the assumption of a plasma temperature profile, which is in general unknown. In this work four possible assumptions for T have been considered: (1) an isothermal corona with constant plasma temperature $T = T_0$; (2) a non-isothermal corona with radial temperature profile

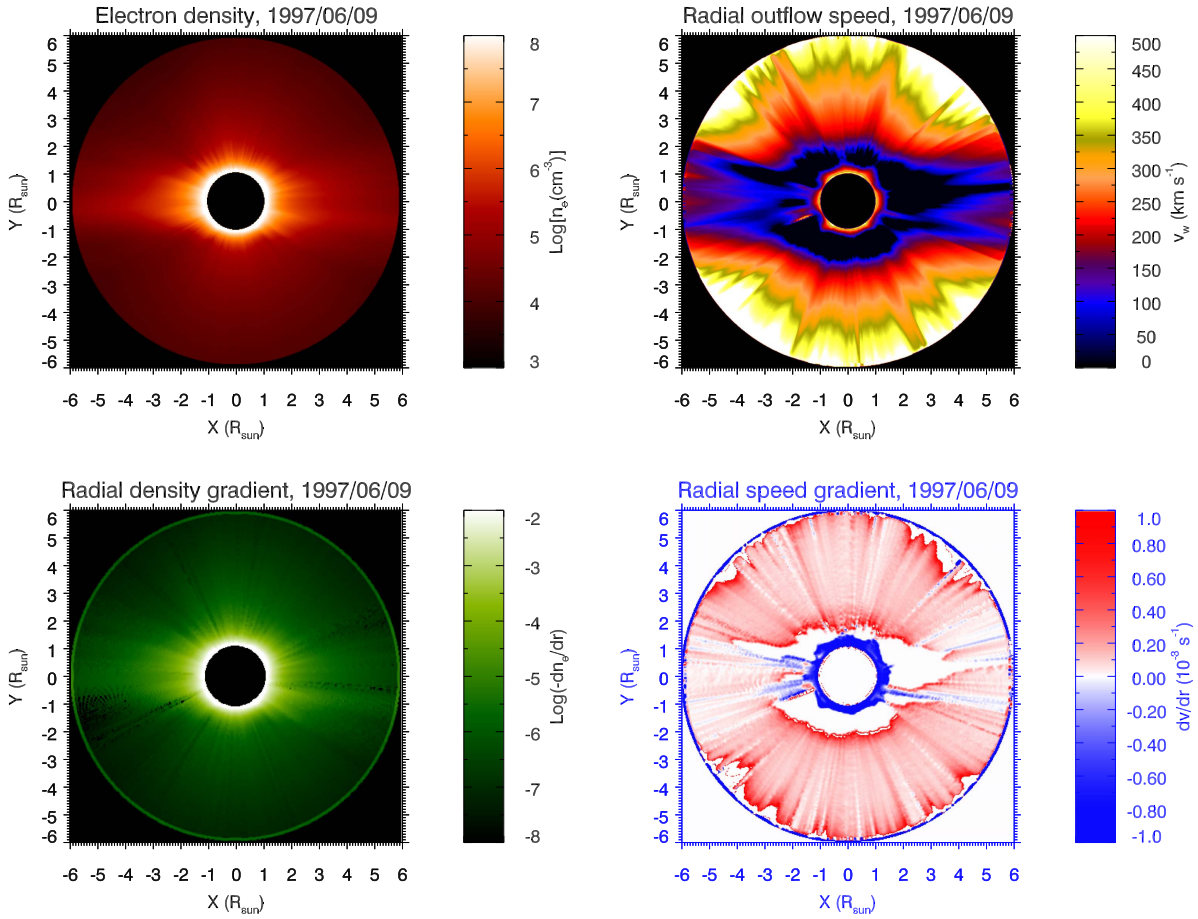

Figure 7. Top: 2D distributions of the electron density (left) and radial outflow speed (right) derived for one selected day during the period analyzed here. Bottom: corresponding 2D distribution of radial density gradient (left) and radial speed gradient for the same day.

given by the classical electron thermal conductivity $T_{\rm cl}(r) = T_0(1/r)^{2/7}$ (with T_0 temperature at the base of the corona, and r expressed in units of $R_\odot$); (3) a non-isothermal corona with temperature profile $T_{\rm eq}(r)$ given by an equatorial radial temperature profile; (4) a non-isothermal corona with temperature profile $T_{\rm po}(r)$ given by a polar radial temperature profile. In particular, here the equatorial and polar radial temperature profiles $T_{\rm eq}(r)$ and $T_{\rm po}(r)$ have been assumed again from Vásquez et al. (2003), according to the analysis described in Section 3. Under the first hypothesis the plasma acceleration $a_{\rm ext} = f_{\rm ext}/\rho$ (resulting from other forces once the gravitational and gas pressure gradient forces are subtracted) is simply given by

$$a_{\rm ext} = v\,\frac{dv}{dr} + \frac{k_B T_0}{\mu\, m_{\rm H}}\frac{1}{\rho}\frac{d\rho}{dr} + G\frac{M_\odot}{r^2}, \tag{8}$$

under the second hypothesis $a_{\rm ext}$ is given by

$$a_{\rm ext} = v\,\frac{dv}{dr} + \frac{k_B T_0}{\mu\, m_{\rm H}}\frac{1}{r^{2/7}}\frac{1}{\rho}\frac{d\rho}{dr} - \frac{2}{7}\frac{k_B T_0}{\mu\, m_{\rm H} R_\odot}\frac{1}{r^{9/7}} + G\frac{M_\odot}{r^2}, \tag{9}$$

while under the third and fourth hypotheses $a_{\rm ext}$ is given by

$$a_{\rm ext} = v\,\frac{dv}{dr} + \frac{k_B}{\mu\, m_{\rm H}}\left(\frac{dT}{dr} + \frac{T}{\rho}\frac{d\rho}{dr}\right) + G\frac{M_\odot}{r^2}. \tag{10}$$

The resulting 2D distributions of the external acceleration $a_{\rm ext}$ derived under the four hypotheses of isothermal (with $T_0 = 2 \times 10^6$ K) and non-isothermal corona are shown in Figure 8 in linear color scale, mapping the distinction between positive (red colors) and negative (blue colors) acceleration regions. The most interesting result in these maps is that, independently of the assumed plasma temperature radial profile, the external acceleration $a_{\rm ext}$ is negative (thus decelerating the wind flux) in the inner corona ($h < 1.8$–2.0 $R_\odot$) and positive (accelerating the wind flux) higher up ($h > 1.8$–2.0 $R_\odot$). This happens unless the classical radial temperature profile $T_{\rm cl}(r) = T_0(1/r)^{2/7}$ is assumed; in the latter case (Figure 8, top right panel) $a_{\rm ext}$ is positive almost everywhere, except in a very thin layer very close to the Sun ($h < 1.1$ $R_\odot$). The acceleration derived with $T_{\rm cl}(r)$ temperature profile is positive almost everywhere because the classical temperature gradient $(dT/dr)_{\rm cl} = -(2/7)(T_0/R_\odot)(1/r^{9/7})$ is negative everywhere even in the inner corona, while the more realistic equatorial $T_{\rm eq}(r)$ and polar $T_{\rm po}(r)$ temperature profiles assumed here have a positive temperature gradient below 1.57 and 1.38 $R_\odot$, respectively, where the temperature reaches a maximum value. Quite unexpectedly, $a_{\rm ext}$ values obtained with the isothermal assumption (Figure 8, top left panel) and with realistic temperature profiles $T_{\rm eq}(r)$ and $T_{\rm po}(r)$ (Figure 8, bottom panels) are very similar. The reason is that in the more general expression for $a_{\rm ext}$ the term going like $\propto dT/dr$ is much smaller than the term $\propto T/\rho\, d\rho/dr$ that dominates for both the equatorial and polar radial temperature profiles assumed here, mainly because the radial variations of temperature are much smaller than the corresponding density variations. For the same

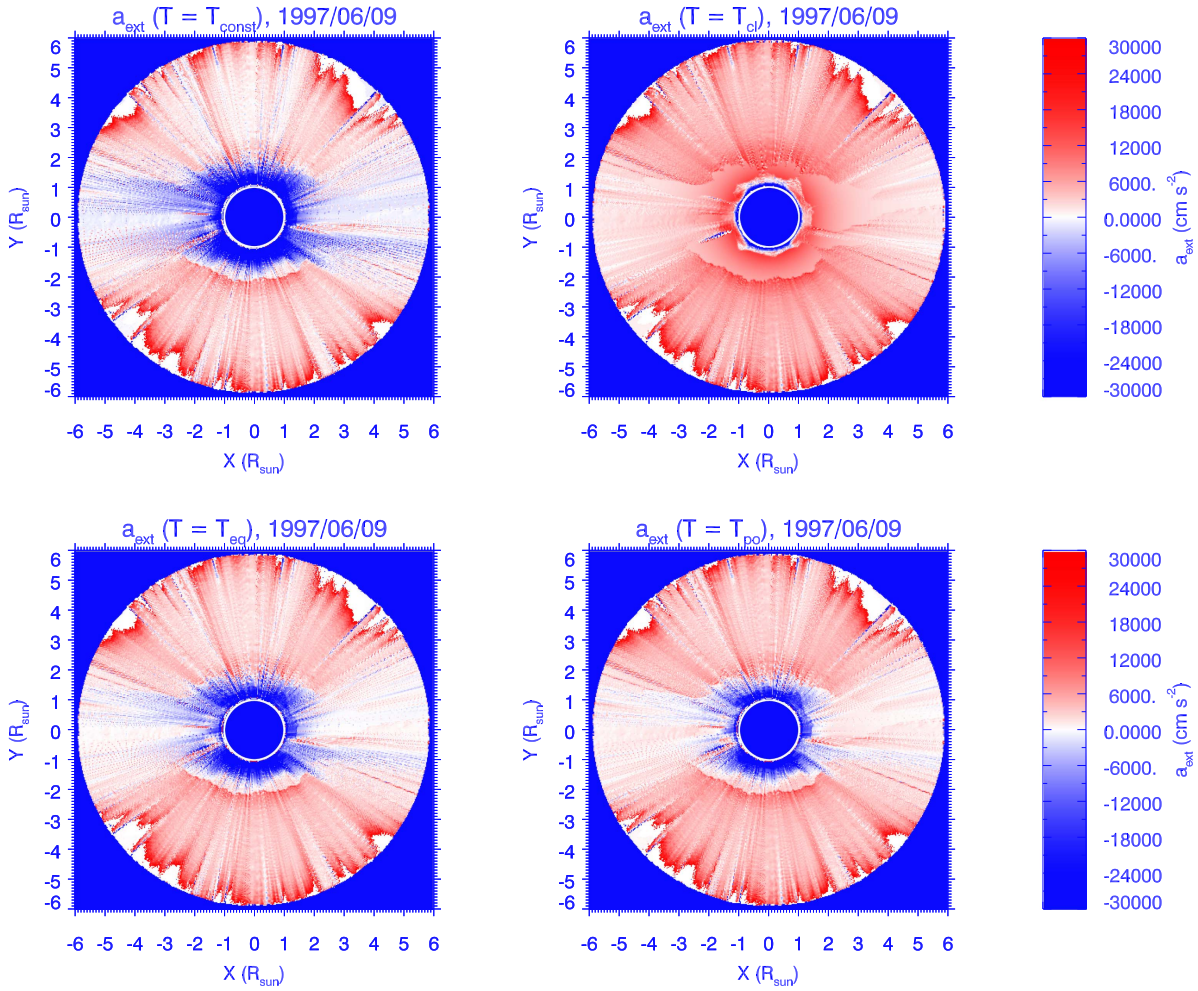

Figure 8. 2D distribution of the external acceleration $a_{\rm ext}$ responsible for plasma deceleration (blue colors) and acceleration (red colors); values of $a_{\rm ext}$ have been computed here by assuming a constant coronal temperature (top left), a radial temperature gradient given by the classical conductivity (top right), and more realistic radial temperature profiles for equatorial streamers (bottom left) and polar coronal holes (bottom right).

reason, because in the term $\propto T/\rho\, d\rho/dr$ the density gradient dominates, $T/\rho\, d\rho/dr \sim T_0/\rho\, d\rho/dr$, and hence results for $a_{\rm ext}$ derived with the two hypotheses are very similar.

The assumptions of the $T_{\rm cl}(r)$ profile, as well as the isothermal assumption, are not realistic and were considered here just for a comparison of $a_{\rm ext}$ values derived with the much more reliable temperature profiles $T_{\rm eq}(r)$ and $T_{\rm po}(r)$. Hence, in the following discussion only $a_{\rm ext}$ values derived with these temperature profiles are considered. Resulting $a_{\rm ext}$ values indicate that solar wind streams originating at active region boundaries and/or in coronal jets (observed, e.g., by *Hinode*/EIS) could be first decelerated in the inner corona, reaching a minimum speed between 0.5 and 2.0 $R_\odot$ above the solar surface, and then reaccelerated again higher up (leading to the solar wind velocities measured, e.g., by UVCS). It is very important to point out here that the altitude where a separation occurs between positive and negative values for $a_{\rm ext}$ is located above the minimum altitude where UV intensities were measured by UVCS, hence in the interpolation (and not extrapolation) region. This means that the location of this very important inversion point is not related to the possible errors due to UV intensity extrapolations at altitudes lower than 1.42 $R_\odot$ discussed above.

Maps in Figure 8 (bottom panels) show many other interesting results. First, the inversion points ($a_{\rm ext} = 0$) are located approximately at the same heliocentric distances $\sim$1.8–2.0 $R_\odot$ for both the equatorial and polar regions. Second, the distribution and radial evolution of $a_{\rm ext}$ values above these inversion points are different, as is also better shown in Figure 9, plotting the radial distribution of $a_{\rm ext}$ around the equatorial (left panel) and the polar (right panel) regions. Below the inversion points ($r < 1.8\ R_\odot$) the coronal plasma undergoes a significant negative acceleration on the order of $|a_{\rm ext}| \sim 10^5$–10^3 cm s^{-2} for both polar and equatorial regions, rapidly decaying with altitude. Then above the inversion point the situation changes: the positive plasma acceleration is almost constant or slightly decreasing in the equatorial region, with a value on the order of $a_{\rm ext} \sim (0.5\text{–}1.0) \times 10^3$cm s^{-2}. In the polar region $a_{\rm ext}$ is much larger immediately above the inversion points ($a_{\rm ext} \sim (5\text{–}8) \times 10^3$ cm s^{-2}) and then, after a decrease with increasing altitude, reaches a constant value on the order of $a_{\rm ext} \sim (2\text{–}3) \times 10^3$ cm s^{-2} above the heliocentric distance of 3 $R_\odot$. Moreover, 2D maps in Figure 8 (bottom panels) indicate that in polar regions the latitudinal distribution of $a_{\rm ext}$ is much more uniform, while in the equatorial regions streams of negative and positive accelerations are mixed quite closely. These major differences (i.e., the absolute $a_{\rm ext}$ values

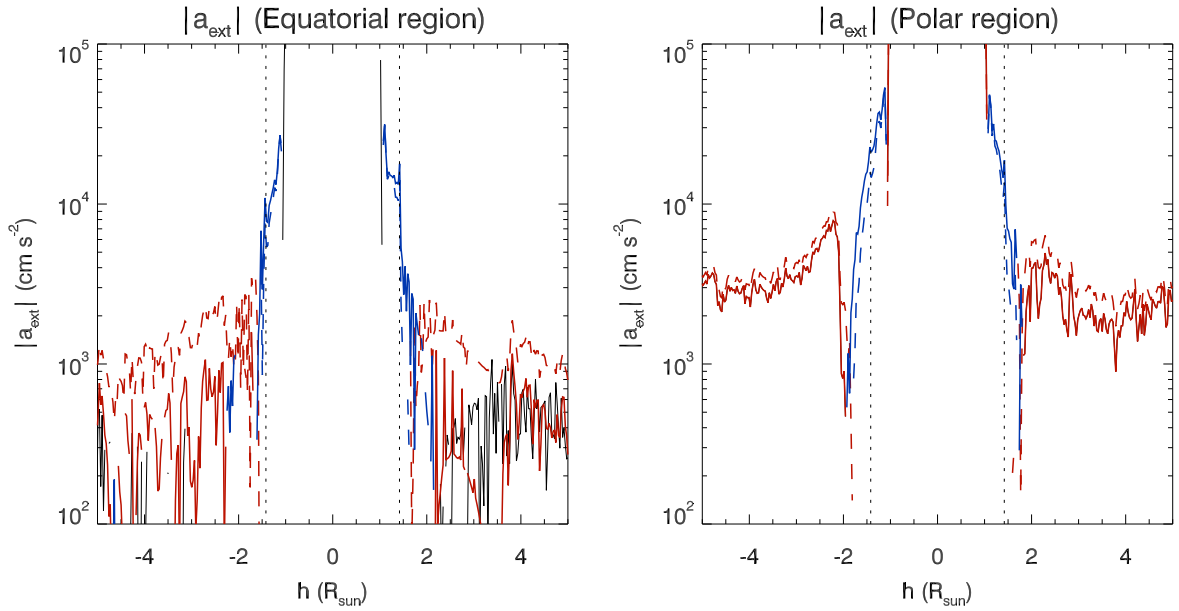

Figure 9. Left: radial distribution of the external acceleration absolute value $|a_{\rm ext}|$ around the equatorial regions as derived with $T_{\rm eq}(r)$ (solid lines) and $T_{\rm po}(r)$ (dashed lines) temperature profiles, and by making a distinction between negative (blue) and positive (red) values. Right: same as in the left panel, plotted around the polar regions. Vertical dotted lines mark the minimum heliocentric distance reached by the UVCS spectrometer during synoptic observations.

above the inversion points, and the latitudinal and radial variations of $a_{\rm ext}$ values) are at the base of the differences between fast and slow solar wind components. Plots in Figure 9 also show that the assumption of the temperature profile is not critical for the determination of the above results.

So far no physical interpretation for $a_{\rm ext}$ values was provided here. It is quite common to assume that the external force $f_{\rm ext}$ is due to a magnetic pressure gradient given by the Alfvén waves, so that $f_{\rm ext} = -dP_{\rm wave}/dr$ with $p_{\rm wave} = \langle \delta B^2 \rangle / 8\pi$ for magnetic field fluctuations δB due to Alfvén waves (integrated over all frequencies), which are in general unknown. These waves are expected to be present in both equatorial and polar coronal regions, characterized by closed or open magnetic field lines, as demonstrated by recent results based on spectropolarimetry showing that the solar corona is pervaded by ubiquitous transverse plasma waves (of fast kink mode type) propagating at all latitudes and altitudes (see review by De Moortel & Nakariakov 2012). By assuming the existence of pure Alfvén waves in the whole corona, the corresponding external acceleration provided by these waves is given by

$$a_{\rm ext} = -\frac{1}{8\pi\ \rho}\frac{d}{dr}\langle \delta B^2 \rangle. \tag{11}$$

With this interpretation, coronal regions where the external acceleration $a_{\rm ext}$ is negative (positive) correspond to regions where the radial gradient of magnetic field fluctuations is positive (negative); hence, the magnetic field fluctuations are increasing (decreasing) with altitude above the solar surface. Because the magnetic field fluctuations are related to Alfvén velocity fluctuations $\langle \delta v_{\rm A}^2 \rangle = \langle \delta B^2 \rangle / (4\pi\ \rho)$, the acceleration $a_{\rm ext}$ is given by

$$a_{\rm ext} = -\frac{1}{8\pi\ \rho}\frac{d}{dr}(\langle \delta v_{\rm A}^2 \rangle 4\pi\ \rho) = -\frac{1}{2}\frac{d\ \langle \delta v_{\rm A}^2 \rangle}{dr} - \frac{\langle \delta v_{\rm A}^2 \rangle}{\rho}\frac{d\rho}{dr} \tag{12}$$

and the inversion point will be located at the altitude where

$$a_{\rm ext} = 0 \longrightarrow -\frac{1}{\rho}\frac{d\rho}{dr} = \frac{1}{2}\frac{1}{\langle \delta v_{\rm A}^2 \rangle}\frac{d\ \langle \delta v_{\rm A}^2 \rangle}{dr}. \tag{13}$$

Hence, the acceleration is negative or positive depending on the relative values of the normalized density gradient $-1/\rho\ (d\rho\ /\ dr) = -\delta_\rho$ compared to one-half of the normalized gradient of the Alfvén velocity fluctuations $(1/2)/\langle \delta v_{\rm A}^2 \rangle d\ \langle \delta v_{\rm A}^2 \rangle / dr = 1/2\ \delta_{v{\rm A}}$. Values of $-\delta_\rho$ are shown in Figure 10 (in linear scale) for the whole 2D corona (left panel) and plotted along the radial direction (in log scale) for the polar and equatorial regions (right panel). The quantity $-\delta_\rho > 0$ is decreasing moving away from the Sun, as expected because the inner corona is characterized by larger density gradients; the quantity $1/2\ \delta_{v{\rm A}} > 0$ (corresponding to a wave amplitude increase with altitude) is expected to decrease as well with altitude, if the Alfvén waves are depositing their energy into the corona. Hence, the inner (outer) coronal region where $a_{\rm ext} < 0$ ($a_{\rm ext} > 0$) could be explained as a region where $-\delta_\rho < 1/2\ \delta_{v{\rm A}}$ ($-\delta_\rho > 1/2\ \delta_{v{\rm A}}$). Figure 10 also shows that the contour level where $-\delta_\rho = 10^{-10}$ cm^{-1} (solid line in the left panel of Figure 10) matches quite well the location of the inversion points (where $a_{\rm ext} \simeq 0$) around the polar regions (see bottom panels of Figure 8). On the other hand, the location of inversion points for equatorial regions corresponds to altitudes where $-\delta_\rho \simeq 5 \times 10^{-11}$ cm^{-1}. These are also the values below which $\delta_{v{\rm A}}$ must get off at different latitudes in order to explain the observed transitions around 1.8–2.0 $R_\odot$ from negative to positive acceleration regions as reported here.

The implications of the above inequalities can be better understood considering that, for wave vertical propagation in a stratified, plane-parallel atmosphere, the Alfvén wave energy

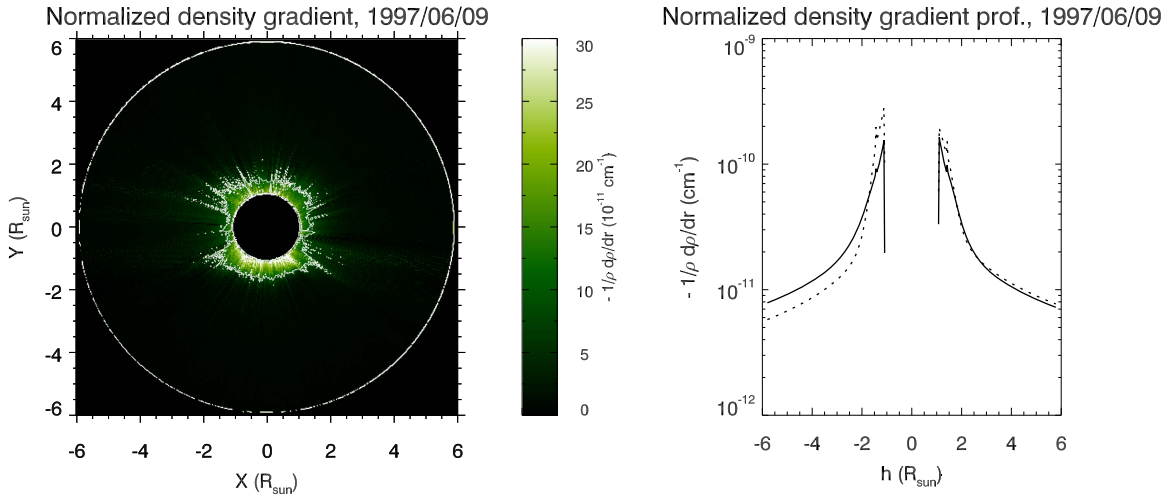

Figure 10. Left: distribution of the normalized density gradient $-1/\rho\ (d\rho/dr)$ at different altitudes and latitudes on 1997 June 9 (log scale); the solid contour corresponds to the level where $1/\rho\ (d\rho/dr) = -10^{-10}$ cm^{-1}. Right: radial variations of the quantity $-1/\rho\ (d\rho/dr)$ along the equatorial (solid lines) and polar (dotted lines) regions.

flux Γ is given by (see, e.g., Moran 2001)

$$\Gamma = \frac{1}{2}\,\rho\,\langle \delta v_{\rm A}^2\rangle\,v_{\rm A} = \frac{1}{4\sqrt{\pi}}\langle \delta v_{\rm A}^2\rangle\,\sqrt{\rho}\,B, \tag{14}$$

and hence the total wave energy flux Γ_t crossing an area with surface S is given by

$$\Gamma_t = \frac{1}{4\sqrt{\pi}}\langle \delta v_{\rm A}^2\rangle\,\sqrt{\rho}(B\,S) = \frac{1}{4\sqrt{\pi}}\langle \delta v_{\rm A}^2\rangle\,\sqrt{\rho}\,\Phi_S(B), \tag{15}$$

where $\Phi_S(B)$ is the magnetic field flux across the magnetic flux tube with cross-sectional area S. Now, if both quantities Γ_t and Φ_S are conserved along the flux tube, then

$$\langle \delta v_{\rm A}^2\rangle = 4\sqrt{\pi}\,\frac{\Gamma_t}{\Phi_S}\,\rho^{-1/2} = K_w\,\rho^{-1/2}, \tag{16}$$

with K_w a constant quantity. Deriving with heliocentric distance r, it turns out that

$$\frac{d}{dr}\langle \delta v_{\rm A}^2\rangle = -\frac{1}{2}K_w\,\rho^{-3/2}\frac{d\rho}{dr} \longrightarrow \frac{1}{\langle \delta v_{\rm A}^2\rangle}\frac{d\,\langle \delta v_{\rm A}^2\rangle}{dr} = -\frac{1}{2\rho}\frac{d\rho}{dr} \tag{17}$$

and hence $\delta_{v\rm A} = -1/2\,\delta_\rho$. This means that in order to have a coronal region where Alfvén waves provide $a_{\rm ext} < 0$, it should be required to have a normalized Alfvén wave amplitude $\delta_{v\rm A}$ four times larger than what is expected in the hypothesis of Alfvén wave energy flux conservation.

Direct comparison with observations is not straightforward: the detection of Alfvénic (and likely not pure Alfvén) waves permeating the lower corona was provided, for instance, by imaging (e.g., Tomczyk et al. 2007; McIntosh et al. 2011) and spectroscopic (Bemporad & Abbo 2012; Hahn & Savin 2013) observations. Nevertheless, the total energy flux associated with these waves can be significantly overestimated by using the classical formula for Γ_t given above: these Alfvénic waves are most probably of fast kink mode type (Van Doorsselaere et al. 2008); hence, their energy flux is heavily influenced by the filling factor, and considering also that we are dealing in general with transverse waves, the above formula likely overestimates Γ_t by a factor of ∼10–50 (Goossens et al. 2013). Nevertheless, by introducing a fraction ϵ_w ($0 < \epsilon_w < 1$) so that the real wave energy flux is only a fraction $\epsilon_w\Gamma_t$, the conservation of this quantity through the corona corresponds again to the same condition $\delta_{v\rm A} = -1/2\,\delta_\rho$ (as far as ϵ_w is constant with the heliocentric distance). Consequences from this discussion are provided in the conclusions.

5. Summary and Conclusions

In this work, a sequence of daily UV (H I Lyα–Lyα) and VL (polarized brightness—pB) coronagraphic data acquired on 1997 June were analyzed in order to derive daily plasma density and outflow velocity 2D maps on the plane of the sky. The UV intensities were acquired by the *SOHO*/UVCS spectrometer, while VL intensities were acquired by the *SOHO*/LASCO-C2 and Mauna Loa MK3 (MLSO) coronagraphs. The main aim of this work was to study for the first time the whole inner solar wind acceleration region from 1 to 6 $R_\odot$ at all latitudes, removing any discontinuity due to gaps between data acquired by different instruments. To this end, the UV intensities acquired by UVCS during synoptic observations have been interpolated between 1.4 and 2.5–3.0 $R_\odot$ and extrapolated at higher and lower heliocentric distances out of this interval. On the other hand, LASCO and MLSO pB images have been combined and interpolated between ∼1.5 and ∼2.5 $R_\odot$. The resulting set of continuous 2D images of UV and VL coronal emissions has then been analyzed with the Doppler dimming and van de Hulst inversion techniques, thus providing daily 2D images of the plasma radial outflow speed and plasma density, respectively.

The derived 2D maps show many interesting characteristics: the speed of the equatorial slow solar wind is highly variable with time and latitude, with respect to the polar fast wind, which is much more stable; this is in nice agreement with the well-known in situ properties of solar wind. Given the 2D distribution of plasma density and outflow speed, corresponding 2D images of wind mass flux have been derived. Significant departures from the mass flux conservation (for a constant flux tube expansion factor) occur below ∼2–3.5 $R_\odot$ at the equator and below ∼1.5–2.5 $R_\odot$ at the poles, thus implying significant super-radial expansions below these intervals, as expected. Larger mass flux decay with distance (and hence most significant super-radial expansion) occurs above the polar regions; this result (in clear

contradiction with the well-known anticorrelation between wind speed and coronal expansion factors found by Wang & Sheeley 1990) could be related to possible overestimates of the outflow speeds derived here near the solar surface. The equatorial regions are characterized at higher altitudes by multiple nearby radial streams with different velocities, in agreement with the more intermittent nature of the slow wind flow as detected in situ with respect to the fast wind; this result also suggests that these nearby streams with different radial speeds are likely related (e.g., via Kelvin–Helmholtz instability) to the origin of the density puffs recently reported by DeForest et al. (2016) with STEREO-HI images.

Clear asymmetries between the wind fluxes at the two poles are observed: below $\sim 3\ R_\odot$ radial speeds above the south pole are systematically lower than those measured above the north pole; on the other hand, while the north pole mass flux is constant above this altitude, the mass flux at the south pole is still slowly increasing with altitude up to at least $6\ R_\odot$, implying that super-radial expansion is still occurring at these distances above the south pole, and not above the north pole. This suggests differences in the magnetic field configurations between the two poles, as supported by other works demonstrating that in the middle period of 1997 the northern coronal hole had a larger area with respect to the southern one (Hess Webber et al. 2014; Lowder et al. 2017), and that globally the northern hemisphere was more active than the southern one (Svalgaard & Kamide 2013). Quite recently Tokumaru et al. (2015) and El-Borie et al. (2016) also found a very small north–south asymmetry in the solar wind speed for year 1997 (i.e., during the rising phase of solar cycle 23), but with a predominance of fast wind at the north pole around the 1996 solar minimum, and the opposite around the solar maximum of 2000. Different mass fluxes between the two poles are likely related to different strengths in the polar magnetic fields, because it is known that the mass flux increases roughly linearly with the footpoint field strength (e.g., Wang 2010).

A very interesting connection was found here between the coronal density and the outflow speed: in the lower corona (below $\sim 1.8\ R_\odot$) these two quantities turn out to be correlated, opposite to what happens higher up, where (in agreement with in situ data) the two quantities are anticorrelated. An empirical relationship is provided here to directly convert a 2D coronal density image into an outflow speed image: this relationship could be used, for instance, to predict in a simple and empirical way the arrival of fast wind streams at Earth, looking from the Lagrangian point L1 at plane-of-sky densities above the east limb, or densities near the Sun–Earth line when a future observatory will be properly located at the Lagrangian point L5 (e.g., Gopalswamy et al. 2011; Lavraud et al. 2016).

This density–speed correlation in the inner corona is also related to the most striking result derived here: the existence of large outflow speed values (>100 km s^{-1}) very close to the Sun. Moving away from the Sun, the outflow speed decreases in both the equatorial and polar regions, reaching a local minimum or possibly a stagnation point, and then slowly increases again, following the typical acceleration profiles measured by previous authors for the slow and fast solar wind components. This behavior has never before been reported: although it is based on the Doppler dimming technique applied to UV intensities that were extrapolated (and not directly observed) below $1.42\ R_\odot$, the local minima in the outflow speed radial profiles are located above this altitude, in the region where the UV intensities were interpolated, and the uncertainties on real values are much smaller. This result is very interesting because over the past ~ 10 yr (as summarized in the Introduction) high-speed flows have been detected at the base of the corona (below $\sim 1.05\ R_\odot$) both around the equator (up to 50 km s^{-1} at the edges of active regions, with a secondary component at $\sim$100–200 km s^{-1}; Sakao et al. 2007; Del Zanna 2008; Hara et al. 2008; Tian et al. 2011a) and in polar coronal holes (up to 60–180 km s^{-1} in plumes, interplumes, and polar jets; Patsourakos & Vial 2000; Gabriel et al. 2003; Tian et al. 2011b). Even if there is no direct physical evidence for bulk (large-scale) outflows in the corona with velocities up to ~ 300 km s^{-1} below $1.4\ R_\odot$ (not including solar eruptions), results presented here provide for the first time a possible connection between small-scale outflows from the base of the corona, possibly due to interchange magnetic reconnection for both the slow (e.g., Fazakerley et al. 2016; Huang et al. 2016) and fast (see discussion by Crooker & Owens 2012) solar wind, and large-scale outflows measured higher up in the intermediate corona. It is also interesting to point out here that an increase in the outflow speed moving closer to the Sun similar to what is described here was recently found below $\sim 2\ R_\odot$ by Imamura et al. (2014) based on an improved radio scintillation technique (see their Figure 9), although these high speeds were attributed by the authors to the crossing of the radio source with fast wind streams.

The 2D distributions of plasma density and outflow speed have been used to derive the corresponding distribution on the plane of the sky of the additional acceleration $a_{\rm ext}$ responsible for the observed behavior, once the gravitational and gas pressure gradient forces are subtracted. Results show that above the inversion points where $a_{\rm ext} \simeq 0$ the slow wind region is characterized by an almost constant or slightly decreasing positive acceleration $a_{\rm ext} \sim 0.5$–1.0×10^3 cm s^{-2}, while in the polar region $a_{\rm ext}$ is much larger immediately above the inversion points ($a_{\rm ext} \sim 5$–8×10^3 cm s^{-2}) and then reaches a constant value on the order of $a_{\rm ext} \sim 2$–3×10^3 cm s^{-2} above the heliocentric distance of $3\ R_\odot$. On the other hand, below the heliocentric distances ~ 1.8–$2.0\ R_\odot$ it turns out that $a_{\rm ext} < 0$ at all latitudes. The negative acceleration in the inner corona derived here could be the same responsible for coronal inflows, seen in coronagraphic images as faint structures propagating downward at $\sim$20–200 km s^{-1} typically below heliocentric distances of $\sim 5\ R_\odot$ (Wang et al. 1999; Sheeley & Wang 2001, 2014). These downflows have been interpreted as the signature of return from the outer corona of open flux (previously injected into the corona by emerging active regions) via field line reconnections occurring below the source surface. Most recently, Tenerani et al. (2016) showed that the inward-propagating signals reported by DeForest et al. (2014) in coronagraphic STEREO/COR2 images are most likely due to reconnection downflows and hence to a large number of reconnection events occurring within the solar wind open flux tubes. The possibility that negative accelerations reported here in the inner corona are related to the same phenomenon cannot be excluded, in principle.

Alternatively, this work tested the possibility that these additional accelerations $a_{\rm ext}$ are provided by magnetic pressure grandients due to Alfvén waves. This scenario implies that the inner (outer) coronal regions with negative (positive) $a_{\rm ext}$ values are characterized by a normalized density gradient

$-1/\rho\ (d\rho/dr) = -\delta_\rho$ being smaller (larger) than one-half of the normalized gradient of the Alfvén velocity fluctuations $1/(2\langle \delta v_A^2\rangle) d\langle \delta v_A^2\rangle/dr = 1/2\ \delta_{vA}$. Values of the latter quantity are quite uncertain in the solar corona; by assuming the propagation of undamped Alfvén (or even Alfvénic) waves through the corona (hence with conservation of magnetic and wave energy fluxes), it turns out that $\delta_{vA} = -1/2\ \delta_\rho$, as was discussed. This leads to the conclusion that in the inner corona a negative acceleration $a_{\rm ext} < 0$ could be explained in terms of plasma waves only if the normalized gradient for wave amplitude δ_{vA} is four times larger than what is implied by the wave energy flux conservation, implying an increase in the wave energy in the lower corona. This conclusion, never reported before, opens the possibility that the plasma, being ejected at high speeds ($v_w > 100$ km s^{-1}) from the base of the corona in active region boundaries or coronal holes, is heated (in a direction perpendicular to the magnetic field) and decelerated (in a direction mostly parallel to the magnetic field) while propagating higher up in the inner corona by the interaction with oblique Alfvén waves. This mechanism has been proposed to explain the interplanetary deceleration of minor ions (Li & Lu 2010) undergoing a preferential heating perpendicular to the magnetic field. The deceleration in the lower corona ($r < 1.8\ R_\odot$) derived here could be due to a similar process, thus providing via momentum transfer additional energy to the plasma waves, increasing their oscillation amplitude and then their energy flux above the level given by wave energy flux conservation. These waves then could propagate higher up ($r > 1.8\ R_\odot$) where v_A becomes significantly larger, thus allowing the waves to reaccelerate again the plasma, leading to the observed intermediate coronal region where $a_{\rm ext} > 0$. In summary, in the interpretation proposed here high-speed plasma outflowing from the base of the corona first "bounces" against oblique Alfvén waves, being heated and decelerated; these waves then propagate higher up, "bouncing" against the plasma and thus leading to its reacceleration and ultimately producing the solar wind flow.

Before concluding, it is important to point out that the whole analysis described was based only on the UV integrated intensities, not taking into account the spectroscopic information in UVCS data. Hence, this work could be considered as a test of what will be possible to do with future data that will be provided by the Metis coronagraph on board the *Solar Orbiter* mission. The two channels of the Metis coronagraph (Antonucci et al. 2012; Fineschi et al. 2012) will observe at the same time the UV (Lyα) and VL (pB) coronal emission with a field of view going from 1.6 to 3.0 $R_\odot$ at minimum perihelion (0.28 au), and from 2.8 to 5.5 $R_\odot$ at 0.5 au. This will allow us for the first time to characterize (without the limitations of the present study, related mainly to UV intensity interpolations and extrapolations) the whole solar wind acceleration region, and how this evolves from short (∼minutes to hours) to long (∼days to years) timescales, thus really providing a new view of the solar corona.

The author acknowledges R. Susino and S. Giordano for valuable help in the selection of UVCS data and in the reconstruction of synoptic observations, as well as L. Abbo and R. Pinto for very useful discussions. The author also aknowledges the anonymous referee for very useful comments. *SOHO* is a mission of international cooperation between ESA and NASA.

ORCID iDs

A. Bemporad https://orcid.org/0000-0001-5796-5653

References

Abbo, L., Ofman, L., Antiochos, S. K., et al. 2016, SSRv, 201, 55
Antonucci, E. 2006, SSRv, 124, 35
Antonucci, E., Dodero, M. A., & Giordano, S. 2000, SoPh, 197, 115
Antonucci, E., Fineschi, S., Naletto, G., et al. 2012, Proc. SPIE, 8443, 844309
Aschwanden, M. J., Poland, A. I., & Rabin, D. M. 2001, ARA&A, 39, 175
Bemporad, A., & Abbo, L. 2012, ApJ, 751, 110
Bemporad, A., Poletto, G., Suess, S. T., et al. 2003, ApJ, 593, 1146
Brooks, D. H., Ugarte-Urra, I., & Warren, H. P. 2015, NatCo, 6, 5947
Brooks, D. H., & Warren, H. P. 2011, ApJL, 727, L13
Cirtain, J. W., Golub, L., Lundquist, L., et al. 2007, Sci, 318, 1580
Cranmer, S. R., Gardner, L. D., & Kohl, J. L. 2010, SoPh, 263, 275
Cranmer, S. R., Kohl, J. L., Noci, G., et al. 1999, ApJ, 511, 481
Cranmer, S. R., Panasyuk, A. V., & Kohl, J. L. 2008, ApJ, 678, 1480
Cranmer, S. R., & van Ballegooijen, A. A. 2005, ApJS, 156, 265
Crooker, N. U., & Owens, M. J. 2012, SSRv, 172, 201
Culhane, J. L., Brooks, D. H., van Driel-Gesztelyi, L., et al. 2014, SoPh, 289, 3799
De Moortel, I., & Nakariakov, V. M. 2012, RSPTA, 370, 3193
de Pontieu, B., McIntosh, S., Hansteen, V. H., et al. 2007, PASJ, 59, S655
DeForest, C. E., Howard, T. A., & McComas, D. J. 2014, ApJ, 787, 124
DeForest, C. E., Matthaeus, W. H., Viall, N. M., & Cranmer, S. R. 2016, ApJ, 828, 66
Del Zanna, G. 2008, A&A, 481, L49
Dolei, S., Spadaro, D., & Ventura, R. 2015, A&A, 577, A34
Dolei, S., Spadaro, D., & Ventura, R. 2016, A&A, 592, A137
El-Borie, M. A., Abdel-halim, A. A., El-Monier, S. Y., & Bishara, A. A. 2016, SoPh, 291, 3817
Fazakerley, A. N., Harra, L. K., & van Driel-Gesztelyi, L. 2016, ApJ, 823, 145
Fineschi, S., Antonucci, E., Naletto, G., et al. 2012, Proc. SPIE, 8443, 84433H
Fu, H., Xia, L., Li, B., et al. 2014, ApJ, 794, 109
Gabriel, A. H., Bely-Dubau, F., & Lemaire, P. 2003, ApJ, 589, 623
Goossens, M., Van Doorsselaere, T., Soler, R., & Verth, G. 2013, ApJ, 768, 191
Gopalswamy, N., Davila, J. M., St., Cyr, O. C., et al. 2011, JASTP, 73, 658
Hahn, M., & Savin, D. W. 2013, ApJ, 776, 78
Hara, H., Watanabe, T., Harra, L. K., et al. 2008, ApJL, 678, L67
Harra, L. K., Sakao, T., Mandrini, C. H., et al. 2008, ApJL, 676, L147
Hess Webber, S. A., Karna, N., Pesnell, W. D., & Kirk, M. S. 2014, SoPh, 289, 4047
Huang, J., Liu, Y. C.-M., Klecker, B., & Chen, Y. 2016, JGRA, 121, 19
Imamura, T., Tokumaru, M., Isobe, H., et al. 2014, ApJ, 788, 117
Kohl, J. L., Esser, R., Gardner, L. D., et al. 1995, SoPh, 162, 313
Kohl, J. L., Noci, G., Antonucci, E., et al. 1997, SoPh, 175, 613
Kohl, J. L., Noci, G., Cranmer, S. R., & Raymond, J. C. 2006, A&ARv, 13, 31
Labrosse, N., Li, X., & Li, B. 2006, A&A, 455, 719
Lavraud, B., Liu, Y., Segura, K., et al. 2016, JASTP, 146, 171
Lemaire, P., Emerich, C., Vial, J.-C., et al. 2002, in Proc. SOHO 11 Symp., From Solar Min to Max, ed. A. Wilson (Noordwijk: ESA Publications Division), 219
Lewis, D. J., & Simnett, G. M. 2000, MNRAS, 317, 1005
Lewis, D. J., & Simnett, G. M. 2002, MNRAS, 333, 969
Li, X., & Lu, Q. M. 2010, JGRA, 115, A08105
Lowder, C., Qiu, J., & Leamon, R. 2017, SoPh, 292, 18
McComas, D. J., Barraclough, B. L., Funsten, H. O., et al. 2000, JGR, 105, 10419
McIntosh, S. W., de Pontieu, B., Carlsson, M., et al. 2011, Natur, 475, 477
Moran, T. G. 2001, A&A, 374, L9
Morgan, H., Fineschi, S., Habbal, S. R., & Li, B. 2008, A&A, 482, 981
Noci, G., & Gavryuseva, E. 2007, ApJL, 658, L63
Noci, G., Kohl, J. L., & Withbroe, G. L. 1987, ApJ, 315, 706
Ofman, L., Abbo, L., & Giordano, S. 2013, ApJ, 762, 18
Paraschiv, A. R., Lacatus, D. A., Badescu, T., et al. 2010, SoPh, 264, 365
Parenti, S., Landi, E., & Bromage, B. J. I. 2003, ApJ, 590, 519
Patsourakos, S., & Vial, J.-C. 2000, A&A, 359, L1
Poletto, G. 2015, LRSP, 12, 7
Raouafi, N. E., Patsourakos, S., Pariat, E., et al. 2016, SSRv, 201, 1
Raouafi, N.-E., & Solanki, S. K. 2004, A&A, 427, 725
Raouafi, N.-E., & Solanki, S. K. 2006, A&A, 445, 735
Richardson, J. D., Wang, C., & Burlaga, L. F. 2003, GeoRL, 30, 2207
Sakao, T., Kano, R., Narukage, N., et al. 2007, Sci, 318, 1585

Scott, S. L., Coles, W. A., & Bourgois, G. 1983, A&A, 123, 207
Sheeley, N. R., Wang, Y.-M., Hawley, S. H., et al. 1997, ApJ, 484, 472
Sheeley, N. R., Jr., & Wang, Y.-M. 2001, ApJL, 562, L107
Sheeley, N. R., Jr., & Wang, Y.-M. 2014, ApJ, 797, 10
Shimojo, M., & Shibata, K. 2000, ApJ, 542, 1100
Sittler, E. C., Jr., & Guhathakurta, M. 1999, ApJ, 523, 812
Spadaro, D., Susino, R., Ventura, R., Vourlidas, A., & Landi, E. 2007, A&A, 475, 707
Strachan, L., Kohl, J. L., Weiser, H., Withbroe, G. L., & Munro, R. H. 1993, ApJ, 412, 410
Strachan, L., Suleiman, R., Panasyuk, A. V., Biesecker, D. A., & Kohl, J. L. 2002, ApJ, 571, 1008
Suleiman, R. M., Kohl, J. L., Panasyuk, A. V., et al. 1999, SSRv, 87, 327
Susino, R., Ventura, R., Spadaro, D., Vourlidas, A., & Landi, E. 2008, A&A, 488, 303
Svalgaard, L., & Kamide, Y. 2013, ApJ, 763, 23
Tenerani, A., Velli, M., & DeForest, C. 2016, ApJL, 825, L3
Teriaca, L., Poletto, G., Romoli, M., & Biesecker, D. A. 2003, ApJ, 588, 566
Tian, H., DeLuca, E. E., Cranmer, S. R., et al. 2014, Sci, 346, 1255711
Tian, H., McIntosh, S. W., De Pontieu, B., et al. 2011a, ApJ, 738, 18
Tian, H., McIntosh, S. W., Habbal, S. R., & He, J. 2011b, ApJ, 736 130
Tokumaru, M., Fujiki, K., & Iju, T. 2015, JGRA, 120, 3283
Tomczyk, S., McIntosh, S. W., Keil, S. L., et al. 2007, Sci, 317, 1192
Tu, C.-Y., Zhou, C., Marsch, E., et al. 2005, Sci, 308, 519
van de Hulst, H. C. 1950, BAN, 11, 135
Van Doorsselaere, T., Nakariakov, V. M., & Verwichte, E. 2008, ApJL, 676, L73
Vásquez, A. M., van Ballegooijen, A. A., & Raymond, J. C. 2003, ApJ, 598, 1361
Vial, J.-C., & Chane-Yook, M. 2016, SoPh, 291, 3549
Wang, Y.-M. 2010, ApJL, 715, L121
Wang, Y.-M., & Sheeley, N. R., Jr. 1990, ApJ, 355, 726
Wang, Y.-M., Sheeley, N. R., Jr., Howard, R. A., Cyr, O. C. S., & Simnett, G. M. 1999, GeoRL, 26, 1203
Withbroe, G. L., Kohl, J. L., Weiser, H., & Munro, R. H. 1982, SSRv, 33, 17
Woo, R., & Martin, J. M. 1997, GeoRL, 24, 2535
Zangrilli, L., & Poletto, G. 2016, A&A, 594, A40
Zangrilli, L., Poletto, G., Nicolosi, P., Noci, G., & Romoli, M. 2002, ApJ, 574, 477